The Compact Muon Solenoid Experiment
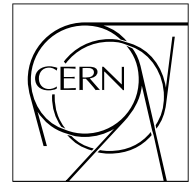
CMS Note

Mailing address: CMS CERN, CH-1211 GENEVA 23, Switzerland

Quark-Gluon Plasma Signatures

R. Vogt[*]

Nuclear Science Division, Lawrence Berkeley National Laboratory, Berkeley, California 94720
and
Physics Department, University of California at Davis, Davis, California 95616 USA

Abstract

Aspects of quark-gluon plasma signatures that can be measured by CMS are discussed. First the initial conditions of the system from minijet production are introduced, including shadowing effects. Color screening of the Upsilon family is then presented, followed by energy loss effects on charm and bottom hadrons, high p_T jets and global observables.

1   Introduction

Finite temperature simulations of lattice gauge theory suggest a phase transition to a new phase of QCD matter—the quark-gluon plasma (QGP). The order of this phase transition depends strongly on the color and flavor degrees of freedom included in the simulations [1]. In a pure SU(N) gauge theory (gluons only), the phase transition is second order, (*i.e.* continuous), for SU(2) and first order (discontinuous) for SU(3). For the gluon theory, the critical temperature, T_c, is 260 MeV. When light quark degrees of freedom are included, the critical temperature is substantially lower with two light flavors, $T_c \approx 170$ MeV, although in this case the phase transition appears to be continuous. For simulations with more light flavors, $n_f \geq 3$, the transition again appears to be first order. However, this conclusion depends on the relative quark masses. The critical energy density is $\epsilon_c \approx 1 - 2$ GeV/fm^3, obtained in simulations both with and without quark degrees of freedom. For a QGP to be formed in ultrarelativistic heavy-ion collisions, the initial temperatures and energy densities must be larger than T_c and ϵ_c. The QGP is expected to be produced in high energy heavy-ion collisions. Significant progress in this field has been made in the last decade at the Brookhaven AGS and the CERN SPS [2]. A dedicated heavy ion collider with Au+Au collisions up to $\sqrt{s} = 200$ GeV per nucleon pair, RHIC [3], is expected to begin operations in April 1999.

Part of the LHC experimental program will be devoted to heavy-ion collisions such as Pb+Pb at $\sqrt{s} = 5.5$ TeV per nucleon pair, the highest energy available for these collisions. This section will focus on possible signature of quark-gluon plasma formation that can be observed with CMS. Two of the most interesting proposed signatures involving hard processes are quarkonium suppression and manifestations of energy loss of fast partons in the medium. A major advantage of the CMS detector is that it is possible to measure both within the same experiment. The ALICE detector [4], dedicated to heavy-ion running, will be able to measure quarkonium suppression up to the Υ family so that some overlap of results is possible even though the acceptances are different. Such cross checks are desirable.

The probability of QGP production and the resulting strength of its signatures depends strongly on the initial conditions. Therefore the first part of this section describes the initial conditions within the context of minijet production. Quarkonium production and suppression is then described with an emphasis on the family of Υ resonances. Charmonium suppression has already been seen in the CERN fixed target program [5], stimulating considerable interest in this topic. However, at the moment the interpretation remains controversial since it has been shown that interactions with hadrons also cause J/ψ suppression, see Ref. [6] for a review, but the anomalous suppression seen in the Pb+Pb data [5] is difficult to explain with hadronic mechanisms alone. Typically, nuclear effects, such as interactions with nucleons and secondary particles which can break up the bound states, are not as strong for Υ production as for the J/ψ [7], perhaps allowing a cleaner interpretation of the Υ data in heavy ion collisions.

The effects of energy loss by fast partons in the medium on heavy quark and jet production is another important signal of dense matter formation that can be measured by CMS. Hard partons interact strongly in the dense matter formed in heavy-ion collisions. The energy lost by these partons during successive interactions has several observable consequences, some of which are discussed here. First, the dilepton continuum above the Υ resonances has important contributions from $c\bar{c}$ and $b\bar{b}$ decays. The relative decay rates depend on the energy lost by the heavy quarks, influencing the content of the dilepton continuum. In addition, the hard jet spectrum is expected to be modified significantly by reinteractions. Particularly, the dijet rate should be suppressed, resulting in an enhancement of monojet production at large jet transverse energy. Finally, although not of least importance, energy loss will also play a role in redistributing global particle production, affecting global variables such as transverse energy production and total multiplicity.

It is important to note that to complete a systematic study of heavy ion collisions and unambiguously determine QGP effects, the signals proposed here should also be studied in pp and pPb collisions at the same energy. Studies with lighter ions such as Ca are also desirable to understand finite volume and energy density effects.

2   Initial Conditions

At the Pb+Pb collision energy perturbative QCD processes are expected to drive the initial conditions. In particular, at early times, $\tau \sim 1/p_T \leq 1/p_0 \sim 0.1$ fm for $p_0 \sim 2$ GeV, semihard production of minijets[1) will set the stage for further evolution of the system [10]. The recent work of Eskola and Kajantie is used to determine the initial conditions from minijet production [11].

[1)] Minijets are jets with $p_T \geq p_0 \sim 1 - 3$ GeV [8], usually not observable as individual jets below $p_T \sim 5$ GeV [9].

The calculation of minijet production is based on the jet cross section for $p_T > p_0$. At leading order, LO, the rapidity distribution of a particular parton flavor in AA collisions is

$$\frac{d\sigma^f}{dy}(\sqrt{s}, p_0) = K \int dp_T^2 dy_2 \sum_{\substack{ij= \\ \langle kl \rangle}} x_1 f_{i/A}(x_1, p_T^2) x_2 f_{j/A}(x_2, p_T^2)$$

$$\times \left[\delta_{fk} \frac{d\hat{\sigma}^{ij \to kl}}{d\hat{t}}(\hat{t}, \hat{u}) + \delta_{fl} \frac{d\hat{\sigma}^{ij \to kl}}{d\hat{t}}(\hat{u}, \hat{t}) \right] \frac{1}{1 + \delta_{kl}} . \tag{1}$$

The parton distributions in the nucleus are normalized to the per nucleon distribution. The limits of integration on p_T^2 and y_2 are $p_0^2 < p_T^2 < s/(4 \cosh^2 y)$ and $\ln(r_{p_T} - e^{-y}) \leq y_2 \leq \ln(r_{p_T} - e^y)$ where $|y| \leq \ln(r_{p_0} + \sqrt{r_{p_0}^2 - 1})$, $r_{p_T} = \sqrt{s}/p_T$ and $r_{p_0} = \sqrt{s}/2p_0$. The sum over initial states includes all combinations of two parton species with three flavors while the final state includes all pairs without a mutual exchange and four flavors (including charm) so that $\alpha_s(p_T)$ is calculated at one loop with four flavors. The final factor, $1/(1 + \delta_{kl})$, is needed to correctly count identical particles in the final state. The parton densities are evaluated at scale p_T, with x values at $y = y_2 = 0$ as low as $x_{1,2} \sim 2p_0/\sqrt{s} \sim 7 \times 10^{-4}$ in Pb+Pb collisions. Thus the small x behavior of the parton densities strongly influences the initial conditions of the minijet system. While the deep inelastic scattering data from HERA [12] continues to refine the parton densities at small x, uncertainties in the distributions still exist. To account for these, results are presented with two different parton distribution sets, GRV 94 LO [13], both because it has a low initial scale and because the LO set is more consistent to use with a LO calculation, and MRS G [14], one of the recent MRS NLO sets. The K factor in eq. (1) indicates the NLO corrections. Previous analysis showed that $K \approx 1.5$ at LHC energies [15]. Assuming $K = 1$, as done in Ref. [11], gives a conservative lower limit.

Other uncertainties are associated with the presence of the nuclear medium. Experiments [16] have shown that the proton and neutron structure functions are modified by a nuclear environment. For momentum fractions $x < 0.1$ and $0.3 < x < 0.7$, a depletion is observed in the nuclear parton distributions. The low x, or shadowing, region and the larger x, or EMC region, is bridged by an enhancement known as antishadowing for $0.1 < x < 0.3$. The entire characteristic modification as a function of x is commonly referred to as shadowing. Therefore to take this effect into account in nucleus-nucleus collisions, the convolution of the parton densities is modified so that

$$f_{i/A}(x_1, p_T^2) f_{j/A}(x_2, p_T^2) \to S^i(A, x_1, p_T^2) f_{i/p}(x_1, p_T^2) S^j(A, x_2, p_T^2) f_{j/p}(x_2, p_T^2) . \tag{2}$$

When $S(A, x, p_T^2) = 1$, there is no shadowing. The shadowing effect is studied with two parameterizations previously used to estimate the effect on heavy quark production in nucleus-nucleus collisions [17] as well as a third, more recent one [18, 19]. All are based on nuclear deep-inelastic scattering data and are averaged over the nuclear volume. The first, $S_1(A, x)$, is based on fits to recent nuclear deep inelastic scattering data [20]. It treats the quark, gluon and antiquark functions equally without Q^2 evolution. The second, $S_2^i(A, x, Q^2)$, separately modifies the valence quark, sea quark and gluon densities and includes Q^2 evolution up to 100 GeV^2 [21] but is based on the Duke-Owens parton distributions [22]. The most recent shadowing parameterization, $S_3^i(A, x, Q^2)$, based on the GRV LO parton distributions [23], evolves each parton distribution separately for $Q^2 \geq 2.25$ GeV^2 [18, 19]. Note that we do not consider the spatial dependence of the parton densities in these calculations but use the average results measured in nuclear deep-inelastic scattering. The possible effects of this spatial dependence have been considered for $c\bar{c}$ and $b\bar{b}$ production [24] and the application to these calculations is in progress [25].

The resulting rapidity distributions are shown in Figs. 1 and 2 for the two sets of parton distributions with and without shadowing. The cross sections are given in units of mb per nucleon pair. Note that the shadowing can reduce the number of produced partons by a factor of two or more, depending on the parameterization and the parton type. The smallest shadowing effect is found with the newer S_3 parameterization. Assuming that the shadowing is independent of impact parameter, the average number of partons produced in a Pb+Pb collision in the CMS acceptance, $|\eta| < 2.4$, can be calculated. In collisions at $\mathbf{b} = \mathbf{0}$, the total number of partons of flavor f is then

$$\overline{N}_{AA}^f(\mathbf{b} = \mathbf{0}, \sqrt{s}, p_0) = 2T_{AA}(\mathbf{b} = \mathbf{0}) \sigma^f(\sqrt{s}, p_0) \tag{3}$$

where $T_{AA}(\mathbf{b})$ is the nuclear overlap function [26] calculated using measured nuclear density distributions [27]. For estimates of conditions in central, $\mathbf{b} = \mathbf{0}$, Pb+Pb collisions, $T_{AA}(\mathbf{0}) \approx A^2/(\pi R_A^2) \propto A^{4/3} = 30.4/\text{mb}$ is used. The transverse area of the system and the initial volume in the nuclear rest frame with the lead radius, $R_{\text{Pb}} = 6.62$ fm, are

$$A_T = \pi R_{\text{Pb}}^2 = 137.8 \text{ fm}^2 \tag{4}$$

$$V_i = A_T \Delta y / p_0 = 65.28 \text{ fm}^3 , \tag{5}$$

2

Figure 1: The rapidity distributions of quarks, antiquarks, gluons and the sum of all contributions in Pb+Pb collisions at $\sqrt{s} = 5.5$ TeV in units of mb per nucleon pair calculated with the GRV 94 LO parton distributions. The solid curve is with no shadowing, the dashed is with shadowing parameterization S_1, the dot-dashed is with parameterization S_2 and the dotted uses S_3. Adapted from [25].
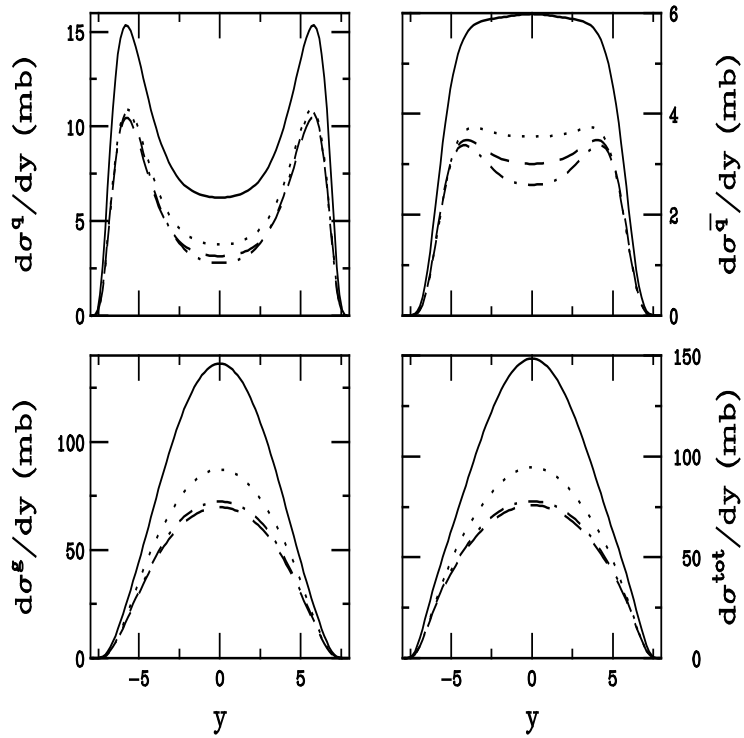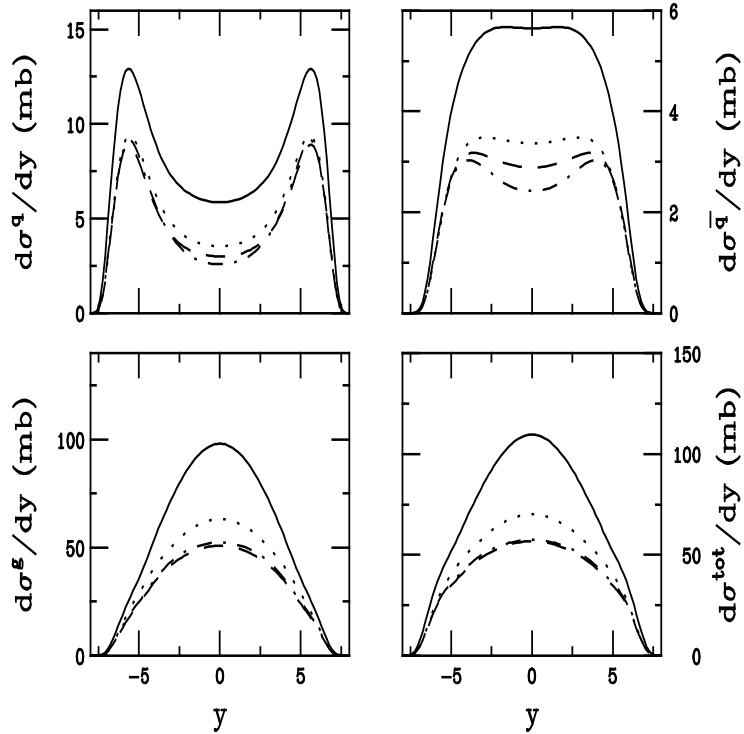

Figure 2: The rapidity distributions of quarks, antiquarks, gluons and the sum of all contributions in Pb+Pb collisions at $\sqrt{s} = 5.5$ TeV in units of mb per nucleon pair calculated with the MRS G parton distributions. The solid curve is with no shadowing, the dashed is with shadowing parameterization S_1, the dot-dashed is with parameterization S_2 and the dotted uses S_3. Adapted from [25].

where $\tau_i = 1/p_0$ with $p_0 = 2$ GeV is used to calculate the volume. The average number of each type of parton in the CMS acceptance is shown in Table 1, with and without shadowing[2].

To further calculate the initial conditions such as the energy density and the produced particle multiplicity, the transverse energy carried by the partons is needed. Estimates of the initial conditions depend on the first E_T moment of each flavor, $\sigma(\sqrt{s}, p_0)\langle E_T^f \rangle$, calculated within the CMS acceptance. A crude approximation of the acceptance is

$$\epsilon(y) = \begin{cases} 1 & \text{if } |y| \le 2.4 \\ 0 & \text{otherwise} \end{cases} . \tag{6}$$

Note that at leading order, the parton pairs are produced back-to-back while at next-to-leading order the angular distribution is somewhat smeared, potentially modifying the E_T moments. The E_T distribution of each flavor is [11]

$$
\begin{aligned}
\frac{d\sigma^f}{dE_T}(\sqrt{s}, p_0) &= \frac{1}{2} \int dp_T^2 dy_2 dy \sum_{\substack{ij= \\ \langle kl \rangle}} x_1 f_{i/A}(x_1, p_T^2) x_2 f_{j/A}(x_2, p_T^2) \frac{1}{1+\delta_{kl}} \\
&\quad \times \left\{ \frac{d\hat{\sigma}^{ij \to kl}}{d\hat{t}}(\hat{t}, \hat{u}) \delta(E_T - [\delta_{fk}\epsilon(y) + \delta_{fl}\epsilon(y_2)] \, p_T) \right. \\
&\quad \left. + \frac{d\hat{\sigma}^{ij \to kl}}{d\hat{t}}(\hat{u}, \hat{t}) \delta(E_T - [\delta_{fl}\epsilon(y) + \delta_{fk}\epsilon(y_2)] \, p_T) \right\} .
\end{aligned}
\tag{7}
$$

The first E_T moment is obtained by integrating eq. (7) over E_T so that

$$
\begin{aligned}
\sigma(\sqrt{s}, p_0)\langle E_T^f \rangle &= \int dp_T^2 dy_2 dy \sum_{\substack{ij= \\ \langle kl \rangle}} x_1 f_{i/A}(x_1, p_T^2) x_2 f_{j/A}(x_2, p_T^2) \frac{1}{1+\delta_{kl}} \\
&\quad \times \left[\delta_{fk} \frac{d\hat{\sigma}^{ij \to kl}}{d\hat{t}}(\hat{t}, \hat{u}) + \delta_{fl} \frac{d\hat{\sigma}^{ij \to kl}}{d\hat{t}}(\hat{u}, \hat{t}) \right] \epsilon(y) p_T .
\end{aligned}
\tag{8}
$$

The E_T moment is given as a function of rapidity in Figs. 3 and 4 both with and without shadowing for the GRV 94 LO and MRS G parton densities. The average transverse energy given to a particular parton species in a central Pb+Pb collision within the CMS acceptance is then

$$\overline{E}_T^f(\mathbf{b}=\mathbf{0}, \sqrt{s}, p_0) = T_{AA}(\mathbf{b}=\mathbf{0}) \, \sigma(\sqrt{s}, p_0)\langle E_T^f \rangle , \tag{9}$$

where $\sigma(\sqrt{s}, p_0)\langle E_T^f \rangle$ is calculated in eq. (8). The energy density of each parton species in a central collision in the CMS acceptance then follows:

$$\epsilon^f = \frac{\overline{E}_T^f(\mathbf{0}, \sqrt{s}, p_0)}{V_i} . \tag{10}$$

The results from eqs. (9) and (10) are given in Table 1 both with and without shadowing. Again, shadowing can reduce the average transverse energy and energy density by up to a factor of two.

In an ideal plasma, the evolution of the energy density is governed by [28]

$$\frac{d\epsilon}{d\tau} + \frac{\epsilon + P}{\tau} = 0 \tag{11}$$

where P is the pressure. There are two extreme cases for the evolution: free streaming, $P = 0$, leading to $\epsilon \sim \tau^{-1}$ and ideal hydrodynamics, $P = \epsilon/3$, where $\epsilon \sim \tau^{-4/3}$. The lower limit of multiplicity is obtained from ideal hydrodynamics where the system is assumed to be in thermal equilibrium at $\tau = 1/p_0 = 0.1$ fm and expands adiabatically with τ. Then the initial entropy determines the final-state multiplicity. The energy and entropy densities are $\epsilon = 3aT^4$ and $s = 4aT^3$ where $a = \gamma_{\text{dof}}\pi^2/90$, proportional to the number of degrees of freedom

---

[2] Note that in these and in the following calculations, including the spatial dependence of shadowing increases the effect at small x in central collisions at this energy [24].
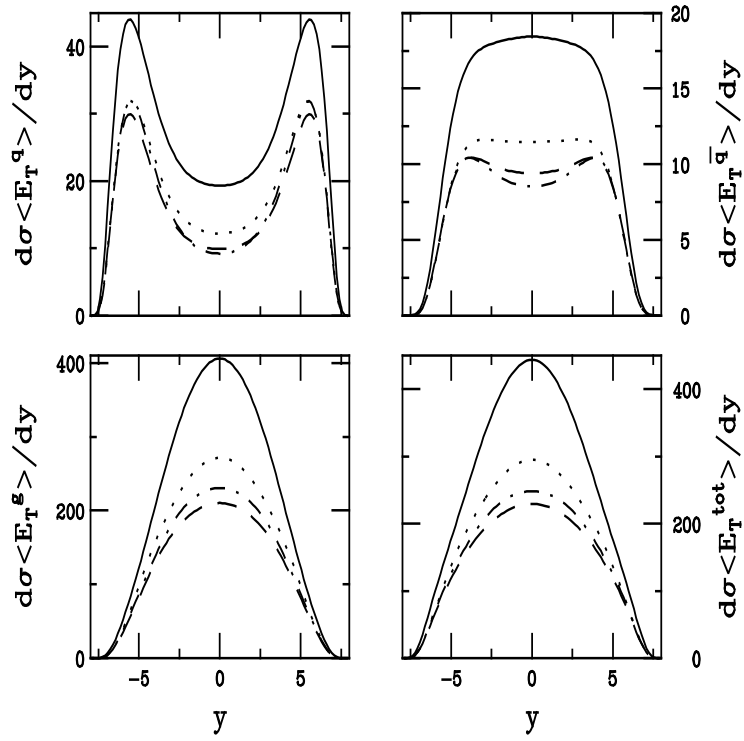
Figure 3: The first E_T moment, $\sigma(\sqrt{s}, p_0)\langle E_T^f \rangle$, as a function of rapidity for quarks, antiquarks, gluons and the sum of all contributions in Pb+Pb collisions at $\sqrt{s} = 5.5$ TeV in units of mb GeV per nucleon pair calculated with the GRV 94 LO parton distributions. The solid curve is with no shadowing, the dashed is with shadowing parameterization S_1, the dot-dashed is with parameterization S_2 and the dotted uses S_3. Adapted from [25].
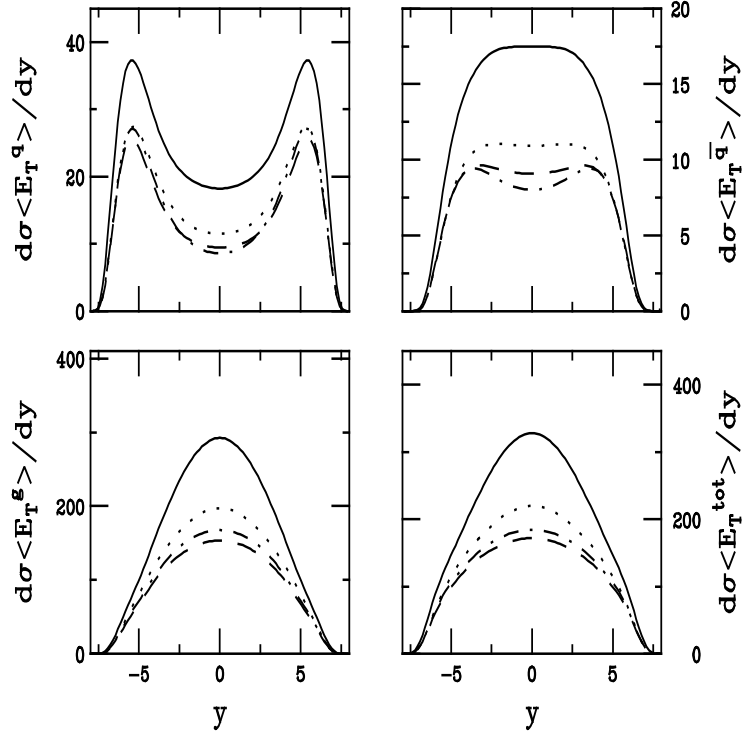
Figure 4: The first E_T moment, $\sigma(\sqrt{s}, p_0)\langle E_T^f \rangle$, as a function of rapidity for quarks, antiquarks, gluons and the sum of all contributions in Pb+Pb collisions at $\sqrt{s} = 5.5$ TeV in units of mb GeV per nucleon pair calculated with the MRS G parton distributions. The solid curve is with no shadowing, the dashed is with shadowing parameterization S_1, the dot-dashed is with parameterization S_2 and the dotted uses S_3. Adapted from [25].

5

	GRV 94 LO				MRS G			
S	q	$\overline{q}$	g	total	q	$\overline{q}$	g	total
$\overline{N}_{\text{PbPb}}(\mathbf{0}, \sqrt{s}, p_0)$								
1	928.5	852.9	18384.7	20166.1	875.1	812.3	13283.6	14971.1
S_1	478.2	439.0	9622.2	10539.7	455.6	422.6	7037.6	7915.9
S_2	437.2	384.5	10015.3	10837.0	405.8	361.8	7277.5	8045.1
S_3	568.6	512.5	11948.7	13029.7	535.6	488.5	8693.5	9717.4
$\overline{E}_T^f(\mathbf{0}, \sqrt{s}, p_0)$ (GeV)								
1	2888.8	2623.9	54534.6	60046.1	2723.6	2499.5	39422.7	44645.4
S_1	1515.0	1372.6	28892.8	31780.2	1444.8	1322.7	21152.9	23920.54
S_2	1460.3	1266.6	31695.0	34421.9	1357.9	1192.6	23076.3	25656.6
S_3	1858.3	1652.2	36957.3	40465.4	1752.6	1576.3	26930.8	30259.6
$\epsilon^f(\mathbf{0}, \sqrt{s}, p_0)$ (GeV/fm^3)								
1	44.25	40.19	835.39	919.82	41.72	38.29	603.9	683.91
S_1	23.21	21.03	442.60	486.83	22.13	20.26	324.0	366.43
S_2	22.37	19.40	485.52	527.30	20.80	18.27	353.5	392.56
S_3	28.47	25.31	566.13	619.88	26.85	24.15	412.5	463.53

Table 1: The average number of partons, eq. (3), average parton transverse energy, eq. (9), and energy density, eq. (10), in central Pb+Pb collisions at $\sqrt{s} = 5.5$ TeV/nucleon within the CMS acceptance. Results are given for both sets of parton distributions used and separated into contributions from quarks, antiquarks and gluons as well as the total. The calculations are done without shadowing, $S = 1$, and with shadowing parameterizations S_1, S_2 and S_3.

with $\gamma_{\text{dof}} = 16$ for a gluon gas and 47.5 for a plasma with gluons and three light quark flavors. The initial temperature can be related to the energy density by

$$T_i = \left(\frac{\epsilon}{3a}\right)^{1/4} . \tag{12}$$

The final multiplicity in the CMS acceptance is then [29]

$$\frac{dN}{dy} \approx \frac{1}{3.6}\frac{dS}{dy} \approx \frac{1}{3.6}\tau_i\pi R_A^2 4aT_i^3 = \frac{4}{3.6}\left[\frac{\tau_i\pi R_A^2 a}{27}\left\{\frac{\overline{E}_T^{\text{PbPb}}(|y| \leq 2.4)}{\Delta y}\right\}^3\right]^{\frac{1}{4}} , \tag{13}$$

where T_i and $\overline{E}_T$ are related by eqs. (10) and (12). The multiplicities and initial temperatures for a pure gluon plasma and a quark-gluon plasma with three quark flavors, calculated with eq. (13), are given in Table 2. Note that for the GRV 94 LO distributions, the total multiplicity at $y = 0$ is $\approx 4000 - 6000$ or about 2700-4000 charged particles. Shadowing reduces the number of charged particles to $\approx 1800 - 2600$. Again, as with the average parton number, the gluon E_T moment dominates the total and drives the rapidity distribution, as can be inferred from Figs. 3 and 4. Note that even though the initial energy density is higher when the quarks are included, the temperature is higher in the gluon plasma since the energy is distributed over fewer degrees of freedom. In either case, T_i is large, nearly 1 GeV for a gluon gas based on the GRV 94 LO parton densities. The initial conditions deduced from minijet production yield significantly larger values of $\epsilon(\tau_i)$ and T_i and, consequently, larger multiplicities than earlier estimates (see *e.g.* [30]). The reason for this is twofold: the fast gluon equilibration time, $\tau_i \sim 1/p_0 \sim 0.1$ fm, and the increase in the parton density at small x as seen at HERA [12]. These high temperatures have important consequences for QGP signatures. Note also that even though shadowing reduces the number of partons and the energy density by up to a factor of two, the corresponding reduction in the multiplicity is lower and the initial temperature is reduced by only 10-15% when shadowing is included, as can be seen in Table 2.

Minijet production thus tends to enhance the probability of QGP production in thermal equilibrium. Effects like shadowing reduce the initial energy density and temperature, taking the system further away from equilibrium. A QGP would still be formed, although not an equilibrated plasma. It is important to determine the effects of minijet production and shadowing on the proposed plasma signatures.

3 Quarkonium Production and Suppression in CMS

One of the proposed signatures of the QCD phase transition is the suppression of quarkonium production [31, 32]. Suppression of the J/ψ and ψ' has been observed in nucleus-nucleus collisions at the CERN SPS [5]. In a QGP, the suppression occurs due to the shielding of the $c\overline{c}$ binding potential by color screening, leading to the

	GRV 94 LO		MRS G	
S	g	total	g	total
		dN/dy		
1	4004.6	5649.3	3139.5	4523.4
S_1	2486.8	3505.5	1968.3	2832.8
S_2	2665.6	3721.7	2101.0	2983.0
S_3	2991.1	4201.9	2359.0	3378.9
		T_i (MeV)		
1	1051	820	969	762
S_1	897	699	829	652
S_2	918	714	848	663
S_3	954	743	881	691

Table 2: The total multiplicity, eq. (13), and initial temperature, eq. (12), within the CMS acceptance. Results for gluons alone as well as for the total are given for both sets of parton distributions. The calculations are done without shadowing, $S = 1$, and with shadowing parameterizations S_1, S_2 and S_3.

breakup of the resonance. The $c\bar{c}$ and $b\bar{b}$ resonances have smaller radii than light-quark hadrons and therefore need higher temperatures for the quarkonium states to break up. At current energies, the situation for the J/ψ is rather ambiguous because the bound state can also break up through interactions with nucleons and comoving hadrons—QGP production has not been proved to be the unique explanation of J/ψ suppression even though an increased density of secondary production is needed, see [6]. Because the Υ is much smaller than the $c\bar{c}$ and other $b\bar{b}$ resonances, a much higher temperature is needed to dissociate the Υ [32]. Therefore it was previously assumed that the Υ would not be suppressed by QGP production [32, 33]. However, in view of the high initial temperature of a gluon plasma, $T \sim 0.9 - 1$ GeV, as shown in Table 2, it was recently shown that, depending upon the properties of the plasma, the Υ could be suppressed, providing a valuable tool to determine the initial state of the system and the characteristics of the plasma [34].

At zero temperature, the massive $Q\overline{Q}$ bound states of charmonium and bottomonium can be described by a nonrelativistic potential model with a linear confining term and a Coulomb-like one gluon exchange term. The quarkonium mass, radius and formation time at $T = 0$ are given in Table 3.

	J/ψ	ψ'	$\chi_c(1P)$	Υ	Υ'	$\chi_b(1P)$
M (GeV)	3.07	3.698	3.5	9.445	10.004	9.897
r (fm)	0.453	0.875	0.696	0.226	0.509	0.408
τ_F (fm)	0.89	1.5	2.0	0.76	1.9	2.6
μ_D (GeV)	0.699	0.357	0.342	1.565	0.671	0.558

Table 3: Properties of the quarkonium states both at $T = 0$ and $T = T_D$, taken from Ref. [32]. The masses, radii and formation times at $T = 0$ are obtained by solving the Schrodinger equation [32]. The value of T_D is determined by the functional form of $\mu(T)$. The screening mass at breakup, μ_D does not depend on the functional form.

In a high temperature environment, the quarkonium binding energy may be reduced due to color screening where the screening mass, $\mu(T)$, is a function of temperature [32]. Minimizing the quarkonium energy at each temperature gives the radius of the bound state as a function of T. For $\mu(T)$ above the critical value, μ_D, there is no longer a minimum and the screening has become strong enough to prevent the formation of the resonance at temperature T_D where $\mu(T_D) = \mu_D$. The values of μ_D for the quarkonium states are also given in Table 3. The actual values of T_D depend upon the functional form of $\mu(T)$.

Perturbative estimates of the screening suggest that $\mu(T) \propto gT$ [35],

$$\frac{\mu(T)}{T_c} = \sqrt{1 + \frac{n_f}{6}} \, g\left(\frac{T}{T_c}\right) \frac{T}{T_c} \tag{14}$$

where the temperature-dependent running coupling constant is

$$g^2\left(\frac{T}{T_c}\right) = \frac{48\pi^2}{(33 - 2n_f)\ln F^2} \, , \tag{15}$$

with $F = K(T/T_c)(T_c/\Lambda_{\overline{MS}})$ and K is also in principle temperature dependent [36]. In SU(3) gauge theory, $T_c = 260$ MeV [37] and $T_c/\Lambda_{\overline{MS}} = 1.03 \pm 0.19$ [38]. A fit to the heavy quark potential in the high temperature limit, $T \gg T_c$, yields the constant $K \approx 33.8$ [36]. Lattice results with $n_f = 2$ and 4 suggest $T_c = 170$ MeV

and $T_c/\Lambda_{\overline{MS}} = 1.05$ [38]. Realistically, the high temperature limit is probably invalid for $T/T_c \leq 3.5$ [39]. Then fitting K to lattice results for $T \geq T_c$ yields [36],

$$K(T/T_c) = \frac{18}{18.4e^{-0.5(T/T_c)^2} + 1} \ . \tag{16}$$

The lower values of $K(T/T_c)$ near T_c results in larger values of $\mu(T)$, suggesting $T_D = T_c$ for all states except the Υ. As shown in Fig. 5 for $n_f = 3$, the two different limiting assumptions of K produce similar results for $\mu(T)$ when $T/T_c \geq 3$ even though below this ratio, they are quite different.
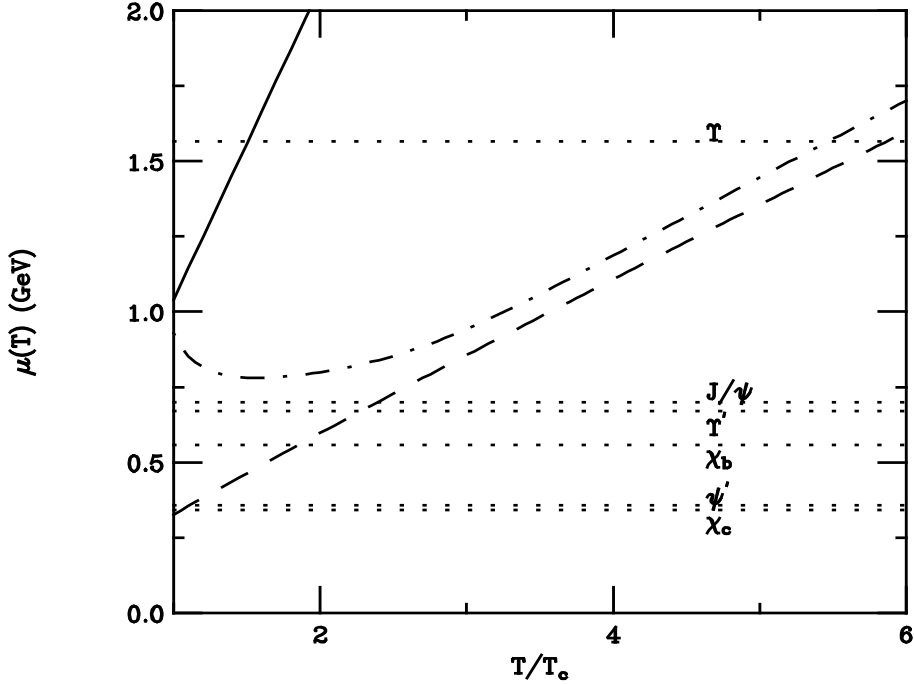

Figure 5: The screening mass as a function of temperature for eq. (17) with $T_c = 260$ MeV (solid). The dashed and dot-dashed curves take $\mu \propto gT$, eq. (14), with $n_f = 3$ in the high temperature limit and the low T fit, eq. (16) respectively. The values of μ_D for the quarkonium states are indicated by the dotted lines. From [6].

In their prediction of J/ψ suppression, Matsui and Satz [31] used a parameterization based on SU(N) lattice simulations [40],

$$\frac{\mu(T)}{T_c} \simeq 4\frac{T}{T_c} \tag{17}$$

which produces values of T_D similar to the results with eq. (16) except for the Υ. This parameterization is also shown in Fig. 5 for $T_c = 260$ MeV.

Due to the uncertain behavior of $\mu(T)$ above T_c, the suppression hierarchy of the quarkonium states in several possible scenarios, described below, is given. The values obtained for T_D in each case are shown in Table 4.

			T_D (MeV)		
	$n_f = 2$	$n_f = 3$	$n_f = 4$	$n_f = 0$	eq. (17)
J/ψ	451	406	366	541	260
ψ'	211	189	170	260	260
χ_c	185	178	170	260	260
Υ	1105	994	901	1326	391
Υ'	434	386	352	512	260
χ_b	350	314	282	416	260

Table 4: The values of T_D for the two choices of $\mu(T)$, eq. (14) from perturbative estimates assuming the high-temperature limit and the pure gluon SU(N) case with $n_f = 0$, eq. (17).

Two cases are chosen for further illustration: I) $n_f = 3$ in the high-temperature limit and IV) $T_D = T_c = 260$ MeV ($n_f = 0$ and SU(3)), eq. (17).

8

As a first step toward studying color screening with the Υ family, it must be determined if the Υ production rate is large enough for the suppression measurement to be feasible. To do this, the phenomenologically successful color evaporation model [41] is used. In this model, the $Q\overline{Q}$ pair neutralizes its color by interaction with the collision-induced color field—"color evaporation". The Q and the $\overline{Q}$ either combine with light quarks to produce heavy-flavored hadrons or bind with each other in a quarkonium state. The additional energy needed to produce heavy-flavored hadrons is obtained nonperturbatively from the color field in the interaction region. Depending on m_b, the yield of all bottomonium states may be only a small fraction of the total $b\overline{b}$ cross section below the $\sqrt{\hat{s}} = 2m_B$ threshold. At leading order,

$$\tilde{\sigma}(s) = \sum_{i,j} \int_{4m_b^2}^{4m_B^2} d\hat{s} \int dx_1 dx_2 \, f_{i/p}(x_1) \, f_{j/p}(x_2) \, \sigma_{ij}(\hat{s}) \, \delta(\hat{s} - x_1 x_2 s) \, , \tag{18}$$

where $ij = q\overline{q}$ or gg and $\sigma_{ij}(\hat{s})$ is the $ij \to b\overline{b}$ subprocess cross section. The color evaporation model was taken to next-to-leading order (NLO) using exclusive $Q\overline{Q}$ hadroproduction [42] to obtain the energy, x_F, and p_T-dependence of quarkonium production [43, 44]. In the color evaporation picture, gg scattering followed by the splitting $g \to b\overline{b}$ incorporated at NLO is similar to models of $g \to \Upsilon$ fragmentation [54]. By including this splitting, the color evaporation model provides a good description of the quarkonium p_T distributions.

The division of $\tilde{\sigma}$ into heavy-flavored hadrons and quarkonium as well as the relative quarkonium production rates are parameters in the color evaporation model. Once these parameters have been determined for a system, the model has significant predictive power if the relative quarkonium production rates are independent of projectile, target, and energy. This appears to be true for the charmonium ratios χ_c/ψ and ψ'/ψ over a broad energy range [45, 46, 47, 48]. The available bottomonium data also follows this trend: $\Upsilon'/\Upsilon = 0.53 \pm 0.13$ and $\Upsilon''/\Upsilon = 0.17 \pm 0.06$ for pp interactions at 400 [49] and 800 GeV [50, 51] and in $p\overline{p}$ collisions at the Tevatron, $\sqrt{s} = 1.8$ TeV [52]. The color evaporation model also reproduces the energy dependence of charmonium and bottomonium production as well as most of the x_F dependence of the charmonium states[3]. The Tevatron charmonium and bottomonium p_T data are also in good agreement with the model at NLO [44].

Using the measured Υ'/Υ and Υ''/Υ ratios, the normalization of each quarkonium state can be fixed empirically from data, allowing predictions of the production cross sections at LHC energies.

First, the model is compared with existing $pp/p\overline{p}$ data. Fixed target Υ data have generally given the sum of Υ, Υ', and Υ'' production, especially if the mass resolution is not good enough to clearly separate the peaks. From the cross section at $y = 0$, $B(d\sigma/dy)_{y=0}$, where B is an effective dilepton branching ratio from all states, a good fit to the data [49, 50, 51, 55, 56] is obtained with

$$B \left(\frac{d\sigma(s)}{dy} \right)_{y=0} = 1.33 \, \times 10^{-3} \, \left(\frac{d\tilde{\sigma}(s)}{dy} \right)_{y=0} \, . \tag{19}$$

The cross section $d\tilde{\sigma}/dy$ is computed using the MRS G [14] and GRV 94 LO [13] parton densities with $m_b = 4.75$ GeV and the renormalization and factorization scales set to $\mu = m_{T,b\overline{b}} = \sqrt{m_b^2 + (p_{T,b}^2 + p_{T,\overline{b}}^2)/2}$ reflecting the production yield through the Υ, Υ', and Υ'' resonances. As shown in Fig. 6, from Ref. [43] with updated parton densities, the high energy data from UA1 [57] and CDF [52] also agree with the energy dependence of the color evaporation model, as obtained from eq. (18). The MRS G distributions produce a better fit to the data than the GRV 94 LO densities, as may be expected since the NLO parton density is more compatible with the NLO calculation. The GRV 94 LO densities are included since they were used to determine the initial conditions. However, the predictions of the Υ yield will be given with the MRS G densities.

The indirect Υ, Υ' and Υ'' components are extracted separately using the Υ'/Υ and Υ''/Υ ratios, and the known branching ratios $B_{\Upsilon_i} \equiv B(\Upsilon_i \to \mu^+\mu^-)$ where Υ_i represents the individual Υ states. If $d\sigma_{\Upsilon_i}/dy|_{y=0} \equiv f_{\Upsilon_i}^{\rm in} d\tilde{\sigma}/dy|_{y=0}$ for the Υ_i cross sections, then from eq. (19),

$$f_{\Upsilon}^{\rm in} B_{\Upsilon} + f_{\Upsilon'}^{\rm in} B_{\Upsilon'} + f_{\Upsilon''}^{\rm in} B_{\Upsilon''} = B = 0.00133 \, . \tag{20}$$

Using $f_{\Upsilon'}^{\rm in}/f_{\Upsilon}^{\rm in} = \Upsilon'/\Upsilon = 0.53$ and $f_{\Upsilon''}^{\rm in}/f_{\Upsilon}^{\rm in} = \Upsilon''/\Upsilon = 0.17$ [49, 50, 51, 52] and B_{Υ_i} [58],

$$f_{\Upsilon}^{\rm in} = 0.038 \, , \quad f_{\Upsilon'}^{\rm in} = 0.02 \, , \quad f_{\Upsilon''}^{\rm in} = 0.0065 \, , \tag{21}$$

---

[3] At high x_F, other production mechanisms such as intrinsic heavy quarks [53] may be important. Additionally, the x_F dependence in nuclear targets is non-trivial.
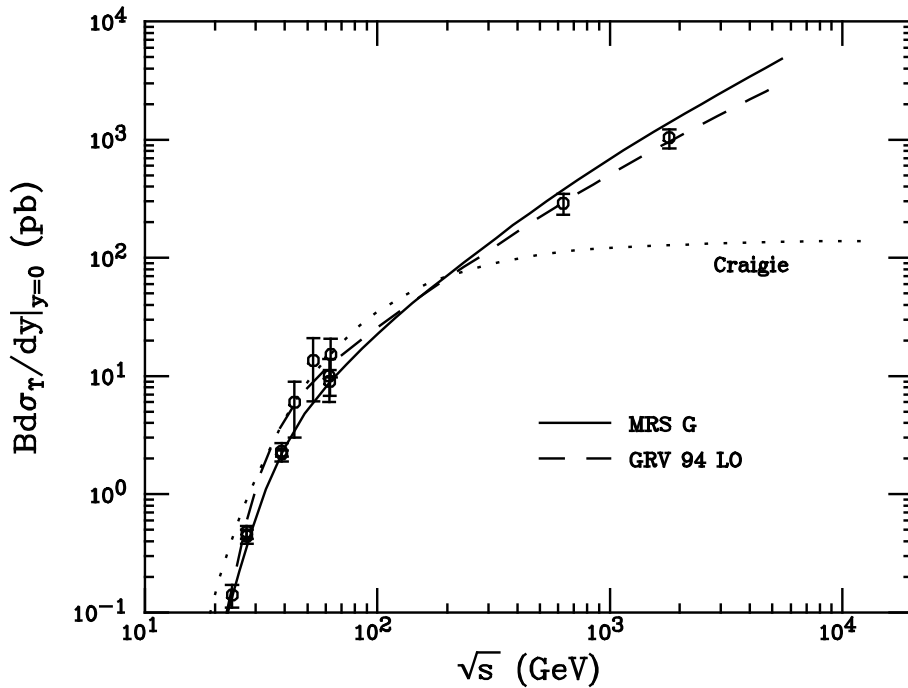
9

Figure 6: We show $Bd\sigma/dy|_{y=0}$ for $\Upsilon + \Upsilon' + \Upsilon''$ in pp collisions, as indicated in eq. (19), for the MRS G [14] (solid) and GRV 94 LO [13] (dashed) parton densities. The data are taken from [49, 50, 52, 55, 56, 57]. This figure is updated from Ref. [43].

slightly smaller than found in Ref. [44], perhaps due to the difference in the small x behavior of the parton densities.

Finally, direct and indirect production are separated. The measured Υ_i production cross sections, or equivalently $f^{\rm in}_{\Upsilon_i}$, are only effective values which reflect both direct production and chain decays of higher mass states. For each i, we assume

$$f^{\rm d}_{\chi_{bi}(1P)} = f^{\rm in}_{\Upsilon'}\,; \quad f^{\rm d}_{\chi_{bi}(2P)} = f^{\rm in}_{\Upsilon''}\,, \tag{22}$$

where $i = 0, 1, 2$ labels the χ_b states in Particle Data Group notation [58], and $f^{\rm d}_{\Upsilon_i}$ indicates the fraction of $\tilde{\sigma}$ from *direct* production. With this and the summed branching ratios [58]

$$\sum_{i=0,1,2} B(\chi_{bi}(1P) \to \Upsilon\gamma) \sim 0.63\,,$$

$$\sum_{i=0,1,2} B(\chi_{bi}(2P) \to \Upsilon\gamma) \sim 0.16\,,$$

$$\sum_{i=0,1,2} B(\chi_{bi}(2P) \to \Upsilon'\gamma) \sim 0.42\,,$$

along with $B(\Upsilon' \to \Upsilon X) \sim 0.27$ and Υ'' decays to Υ', Υ and $\chi_{bi}(2P)$, the $f^{\rm d}_{\Upsilon_i}$'s for direct production can be found for all the Υ_i. About 0.013 of the total $f^{\rm in}_{\Upsilon} = 0.038$ is due to $\chi_{bi}(1P)$ decays, similar to the analogous ψ and χ_c fractions. Similarly, ~ 0.001 of $f^{\rm in}_{\Upsilon}$ and ~ 0.0027 of $f^{\rm in}_{\Upsilon'}$ would be due to $\chi_{bi}(2P)$ decays. Also important are $\Upsilon' \to \Upsilon X$ decays; from eq. (21), $f^{\rm in}_{\Upsilon'}$ implies that an additional 0.0054 of $f^{\rm in}_{\Upsilon}$ would be indirect. The contributions from chain decays of the Υ'' are small. Also, there are no contributions to the Υ'' rate coming from higher states that are known to be significant. Altogether:

$$f^{\rm d}_{\Upsilon} \sim 0.019,\ f^{\rm d}_{\Upsilon'} \sim 0.017,\ f^{\rm d}_{\Upsilon''} \sim 0.0065\,,$$
$$f^{\rm d}_{\chi_{bi}(1P)} \sim 0.020,\ f^{\rm d}_{\chi_{bi}(2P)} \sim 0.0065\,, \tag{23}$$

where $i = 0, 1, 2$ labels the different $\chi_{bi}(1P, 2P)$ states. Note that only about half of $f^{\rm in}_{\Upsilon}$ is due to direct Υ production.

In Table 5, the corresponding normalized direct production cross sections in pp collisions, $f^{\rm d}\tilde{\sigma}_{pp}$, are given for each state with $f^{\rm d}$ from eq. (23) and $\tilde{\sigma}_{pp}$ computed using the MRS G parton densities at $\sqrt{s} = 5.5$ TeV/nucleon.

10

	Υ	Υ'	Υ''	$\chi_b(1P)$	$\chi_b(2P)$
$f^{\rm d}\tilde{\sigma}_{pp}$ (nb)	301	269	103	316	103
$N^{\rm d}$(central)	1.42×10^6	1.27×10^6	4.87×10^5	1.49×10^6	4.87×10^5
$N^{\rm d}_{\mu\mu}$(central)	3.52×10^4	1.66×10^4	8.81×10^3	-	-
$N^{\rm d}$(min bias)	7.64×10^6	6.28×10^6	2.61×10^6	8.02×10^6	2.61×10^6
$N^{\rm d}_{\mu\mu}$(min bias)	1.89×10^5	8.91×10^4	4.72×10^4	-	-

Table 5: The normalized cross sections, $f^{\rm d}\tilde{\sigma}_{pp}$, for directly produced bottomonium states in pp collisions at $\sqrt{s} = 5.5$ TeV/nucleon, using the direct fractions $f^{\rm d}$ from eq. (23) and the prediction of eq. (18), $\tilde{\sigma}_{pp} = 15.84\,\mu$b, with the MRS G parton densities, $m_b = 4.75$ GeV and $\mu = m_{T,b\bar{b}}$. Also given is the number, $N^{\rm d}$, of each type of bottomonium state directly produced in central, eq. (24), and minimum bias, eq. (25), Pb+Pb collisions. For Υ, Υ' and Υ'' the corresponding number of $\mu^+\mu^-$ pairs from decays of directly produced states, $N^{\rm d}_{\mu\mu}$, is also given for central and minimum bias collisions. Modified from [34].

The cross sections in Table 5 are integrated over all rapidity. When shadowing is included, the rate per nucleon pair decreases 55% with the S_1 parameterization, 30% with $S = S_2$ and 26% with S_3.

The results for $f^{\rm d}\tilde{\sigma}_{pp}$ given in Table 5 in pp collisions can be employed to predict the rates for direct production of bottomonium states in Pb+Pb collisions at the LHC. For central collisions, the expected rates are given by

$$N^{\rm d}(\text{central}) = \sigma_{NN}T_{\rm PbPb}(\mathbf{0})f^{\rm d}\tilde{\sigma}_{pp}L_{\rm int}^{\rm PbPb} \ , \tag{24}$$

where $\sigma_{NN}T_{\rm PbPb}(\mathbf{0}) = 1824$ is the number of central Pb+Pb collisions[4]. The number of Υ states produced in minimum bias collisions (all impact parameters) is

$$N^{\rm d}(\text{min bias}) = A^{2\alpha}f^{\rm d}\tilde{\sigma}_{pp}L_{\rm int}^{\rm PbPb} \ , \tag{25}$$

where $\alpha \approx 0.95$ for Υ production at fixed-target energies [59]. In one month (30 days) of running the integrated luminosity for lead beams is expected to be $L_{\rm int}^{\rm PbPb} = 2.59$/nb assuming that $L^{\rm PbPb} = 1 \times 10^{27}$ cm^{-2}s^{-1}. Typical rates are on the order of 10^6 for Υ and Υ'. Approximately 10-15% of the cross section is within $|\eta| \leq 1$. The number of muon pairs from the Υ, Υ' and Υ'' decays, found by multiplying the total number of Υ_i directly produced in central or minimum bias collisions, $N^{\rm d}$, by the appropriate branching ratio, is also given in Table 5. These rates suggest that production and suppression of these states should be measurable by CMS in the very clean $\mu^+\mu^-$ final state decay mode.

Since the expected rate is large enough to be measurable before color screening is taken into account, predictions of how the Υ rate would be modified by QGP production at the LHC are given. With the high temperatures in Table 2, strong suppression due to QGP formation might be expected. Unfortunately the short equilibration time of the minijet system correspondingly reduces the plasma lifetime in the scaling expansion, causing the minijet plasma to be too short-lived to produce quarkonium suppression in some cases.

Alternatively, the initial conditions could be dominated by kinetic equilibration processes [60] with a correspondingly longer equilibration time, $t_0 \sim 0.5 - 0.7$ fm. This time is reached when the momentum distributions are locally isotropic due to elastic scatterings and the expansion of the system. Chemical equilibrium is generally not assumed but the system moves toward equilibrium as a function of time. Then the cooling of the plasma is more rapid than the simple scaling [28] adopted here, producing incomplete suppression at low p_T. Because the equilibration time of the parton gas is longer than that obtained from the minijet initial conditions, the time the system spends above the breakup temperature is also longer, leading to stronger suppression even though T_0 is lower.

The time at which the temperature drops below T_D and the state can no longer be suppressed, $t_D = t_0(T_0/T_D)^3$, and the maximum quarkonium p_T for which the resonance is suppressed, $p_{T,\rm m} = M\sqrt{(t_D/\tau_F)^2 - 1}$, are given in Table 6 for cases I ($\mu(T) \propto gT$ with $n_f = 3$ in the high temperature limit since $T_0 > 3T_c$) and II ($\mu(T) = 4T$, SU(3) plasma with $T_c = 260$ MeV) with both the parton gas and minijet, Table 2, initial conditions. Results for the minijet initial conditions are given for the GRV 94 LO parton densities for both $S = 1$ and the lowest temperatures obtained with shadowing when $S = S_1$. Note that the reduction of the initial temperature due to shadowing significantly reduces the p_T range of the suppression. However, this result can be distinguished from a case with no significant shadowing and a plasma with a smaller spatial extent [34].

A high statistics study of quarkonium production ratios such as ψ'/ψ and Υ'/Υ as a function of p_T may provide a conclusive test of plasma production at high energies. However, before the efficacity of the measurement as a test

---

[4] Assuming that σ_{NN} rises as $\sigma_{p\bar{p}}$ at high energies, $\sigma_{NN} \approx 60$ mb.

of QGP formation is proven, the relative importance of other effects must be established. Although shadowing is important, the effects should be canceled in ratios of quarkonium states with very similar masses, as can be checked by pA studies. Nuclear absorption would also cancel in the ratios if the quarkonium state interacts with nucleons while still in a preresonance color octet state, as already proposed at fixed-target energies [61]. To complicate matters, the resonances can interact with comoving secondaries. However, even though these cross sections can differ for individual resonances, the p_T dependence of these comover interactions is already weak at CERN SPS energies [62] and expected to be weaker at the LHC [34].

If the ratios exhibit a significant p_T-dependence at large p_T in AB collisions, it will be virtually certain that a quark gluon plasma was formed. The precise behavior of the ψ'/ψ and Υ'/Υ ratios can then be used to strongly constrain the QGP model parameters. In particular, the ratios will be very different if only the Υ' or ψ' is suppressed relative to the case where all quarkonium states are suppressed.

	LHC			
	case I, $n_f = 3$		case II, $T_c = 260$ MeV	
	parton gas			
	$T_0 = 820$ MeV, $t_0 = 0.5$ fm			
	t_D (fm)	p_{Tm} (GeV)	t_D (fm)	p_{Tm} (GeV)
ψ	4.12	13.96	15.69	54.0
ψ'	40.8	100.6	15.69	38.5
χ_c	48.9	85.47	15.69	27.2
Υ	-	0	4.6	56.53
Υ'	4.79	23.16	15.69	81.98
χ_b	8.90	32.42	15.69	58.9
	minijet plasma, $S = 1$			
	$T_0 = 820$ MeV, $t_0 = 0.1$ fm		$T_0 = 1.05$ GeV, $t_0 = 0.1$ fm	
	t_D (fm)	p_{Tm} (GeV)	t_D (fm)	p_{Tm} (GeV)
ψ	-	0	6.59	22.7
ψ'	8.17	19.8	6.59	15.8
χ_c	9.78	16.75	6.59	11.0
Υ	-	0	1.94	22.2
Υ'	-	0	6.59	33.2
χ_b	-	0	6.59	23.05
	minijet plasma, $S = S_1$			
	$T_0 = 699$ MeV, $t_0 = 0.1$ fm		$T_0 = 897$ MeV, $t_0 = 0.1$ fm	
	t_D (fm)	p_{Tm} (GeV)	t_D (fm)	p_{Tm} (GeV)
ψ	-	0	4.11	13.8
ψ'	5.06	11.9	4.11	9.4
χ_c	6.06	10.0	4.11	6.3
Υ	-	0	1.21	11.7
Υ'	-	0	4.11	19.2
χ_b	-	0	4.11	12.1

Table 6: LHC values of t_D, and p_{Tm} with cases I and II for $\mu(T)$ with a parton gas and a minijet plasma with $S = 1$ and S_1 from the GRV 94 LO calculation, adapted from Ref. [34].

In Fig. 7, the ratio of the ψ' and ψ cross sections are shown for several sets of initial conditions. Since it has been demonstrated that the χ_c and ψ' contributions to large p_T J/ψ production can be subtracted at $p\bar{p}$ colliders [45], the direct or 'prompt' ratio is displayed. The parton gas produces suppression over nearly twice the p_T range as the minijet initial conditions, as shown in Table 6. In case II, the ψ is more suppressed than the ψ' for a large range of p_T, up to 54 GeV for the parton gas. In case I, the ψ' is more suppressed than the ψ except when $p_T < 9$ GeV in the parton gas. The kink in the dashed curve appears when the ψ is no longer suppressed. In each case, the p_T signature obvious in the ψ'/ψ production ratios is unique if the full p_T range can be measured. Otherwise it may be difficult to distinguish between the parton gas and minijet plasma initial conditions for $p_T < 20$ GeV at the LHC unless the measurement is made with sufficiently high statistics. Note that even though the decreased initial temperature of the minijet gas when shadowing is included reduces the p_T range of the suppression, the shape of the ratio remains similar.

It is doubtful that the prompt Υ rate can be successfully extracted because the feeding from χ_b states will be difficult to disentangle [63]. The Υ family is also more complex, including feeddown to the Υ from Υ', Υ'' and two sets of χ_b states and feeddown to the Υ' from the Υ'' and $\chi_b(2P)$ states. Thus in the Υ'/Υ ratio, all sources of Υ' and Υ, each associated with a different suppression factor, must be considered [34]:

$$\frac{\Upsilon'}{\Upsilon}\Big|_{\text{indirect}} \equiv \frac{\Upsilon' + \chi_b(2P)(\to \Upsilon') + \Upsilon''(\to \Upsilon')}{\Upsilon + \chi_b(1P, 2P)(\to \Upsilon) + \Upsilon'(\to \Upsilon) + \Upsilon''(\to \Upsilon)} . \tag{26}$$
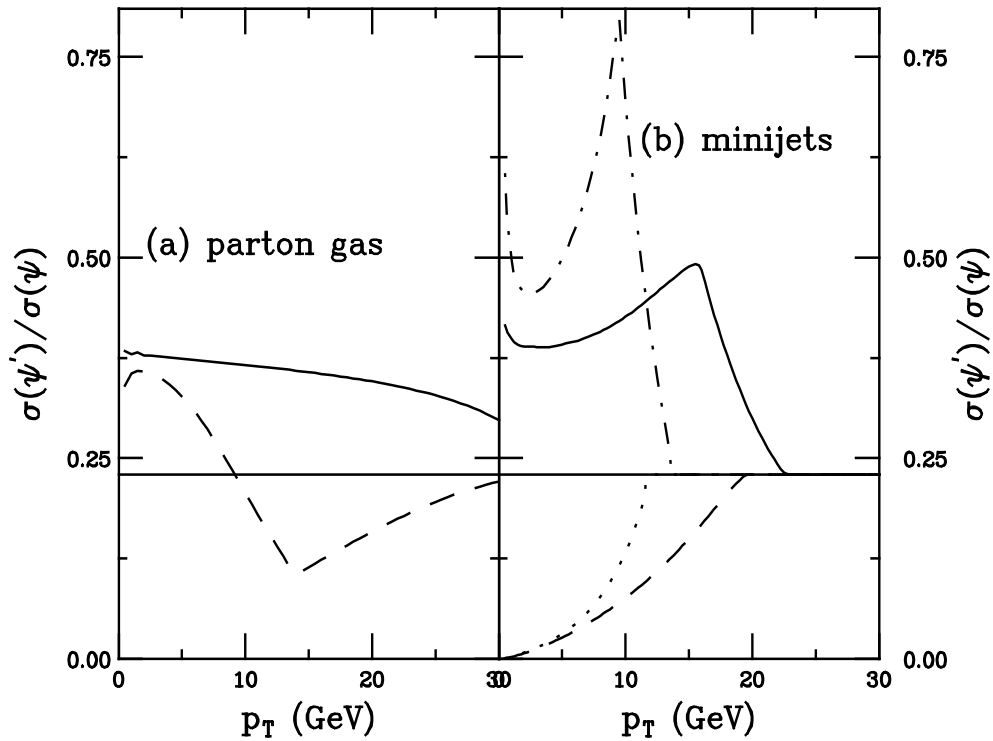
Figure 7: The direct or prompt ψ'/ψ ratio as a function of p_T is shown for several choices of initial conditions and $R = R_{\mathrm{Pb}}$. In (a), parton gas results are shown for case I (dashed) and case II (solid). In (b) minijet results are given for both cases without shadowing, case I (dashed) and case II (solid), and with $S = S_1$, case I (dotted) and case II (dot-dashed). The horizontal curve represents the pp ratio. Modified from [6].
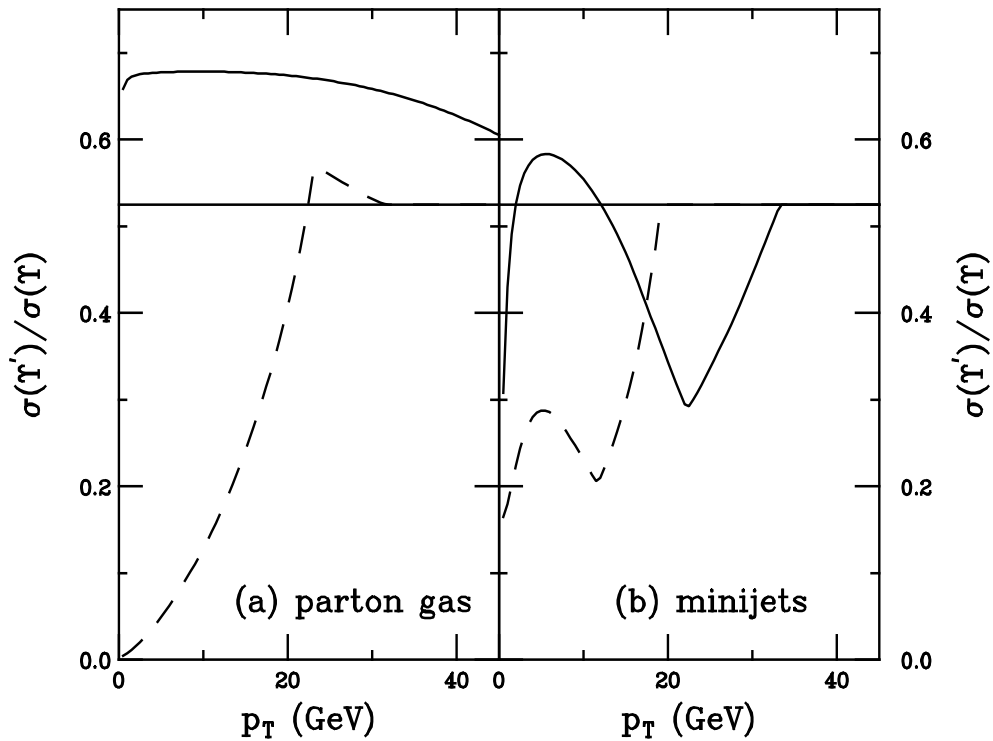

Figure 8: The Υ'/Υ ratio computed from eq. (26) is shown for several initial conditions and $R = R_{\mathrm{Pb}}$. In (a), parton gas results are shown for case I (dashed) and case II (solid). In (b) minijet results are given for case II without shadowing (solid) and with $S = S_1$ (dashed). The horizontal curve represents the pp ratio. Modified from [6, 34].

13

In computing this 'indirect' Υ'/Υ ratio it is assumed that the suppression factor is the same for the $\chi_b(2P)$ and $\chi_b(1P)$ states and that identical suppression factors can be used for the Υ' and Υ''. The relative production and suppression rates in the color evaporation model, including the χ_b states, can be found in Ref. [34].

Figure 8 gives the indirect results. In a parton gas assuming a plasma like case II, all the Υ states can be suppressed for $p_T > 50$ GeV, producing the rather flat ratio given in the solid curve. A measurement at the 20% level is thus needed to distinguish between the pp value of the ratio and the QGP prediction. Substantial systematic errors in the ratio could make the detection of a deviation quite difficult due to the slow variation with p_T. This is a disadvantage of the indirect ratio: the prompt ψ'/ψ ratio is enhanced by nearly a factor of two over the pp value, making detection easier. With the slowly growing screening mass of case I, the direct Υ rate is not suppressed while the Υ' and χ_b states are suppressed. Under these conditions, the indirect ratio is less than the pp value until the Υ' is no longer suppressed and then is slightly enhanced by the χ_b decays until they also no longer suffer from plasma effects. Thus although the indirect ratio is less sensitive to the plasma, the Υ'/Υ and ψ'/ψ ratios together can significantly constrain plasma models, especially if the quarkonium states can be measured with sufficient accuracy up to high p_T. Again, the shape of the ratio is similar when the effect of shadowing on the initial conditions is included although the range of the suppression is reduced.

4   Using the Z as a Baseline

In the current experiments at the CERN SPS, J/ψ production is compared to the dilepton continuum [5, 64]. The continuum is assumed to be produced via the Drell-Yan ($\gamma^\star$, $Z^\star$-exchange) process and is, in fact, Drell-Yan-like. At the LHC, the continuum will be more difficult to understand because of the important contribution from semileptonic $c\bar{c}$ and $b\bar{b}$ decays. Not only are there uncertainties in the total $c\bar{c}$ cross section, but the heavy quark decays are also subject to nuclear effects. The relatively small Drell-Yan contribution is also subject to shadowing effects in the mass range between the J/ψ and the Υ. Another choice is needed. One possibility is Z production. Because the Z is produced in point-like fashion, the difference between the Z p_T-dependence in pp and Pb+Pb collisions will not be influenced by the quark-gluon plasma.

Figure 9 illustrates the cross section for Z production as a function of p_T at $\sqrt{s} = 5.5$ TeV assuming no shadowing. The p_T distribution, $d\sigma/dp_T$, is given for $pp \to ZX$ including the individual contributions from $q\bar{q}$ and $qg + \bar{q}g$ collisions. One-loop corrections to the $Z + jet$ cross section are included[5] but resummation effects are not. To obtain the number of events per month per GeV in central collisions, multiply by $\sigma_{NN}T_{\mathrm{PbPb}}(\mathbf{0})L_{\mathrm{int}}^{\mathrm{PbPb}} = 4.973 \times 10^3$ nb^{-1}. At $p_T = 50$ GeV, the cross section is of order 10^{-3} nb/GeV, implying about 2 events per GeV for 40% acceptance and detection efficiency. Thus, for a 5 GeV bin, about 10 events are found in this bin per month of running. After a year of running, this would yield a statistical accuracy of order 9%. At low p_T, event rates are a factor of ~ 10 larger, yielding correspondingly greater accuracy. The predicted effects of the QGP typically imply survival probabilities that differ by much larger percentages compared to unity. In any case, as estimated earlier, the errors in the measurements of the Υ spectra will be larger. Thus, production rates in the $p_T \lesssim 50$ GeV domain are high enough that $Z \to l^+l^-$ can provide a standard of comparison. It is necessary to also measure Z production in pp collisions at $\sqrt{s} = 5.5$ TeV to determine if shadowing and other nuclear effects influence the Pb+Pb spectra. Good statistical accuracy for up to $p_T = 50$ GeV requires an integrated luminosity for pp collisions of order $L = 0.01$ fb^{-1}, which should be easily achieved in a few weeks of running.

The two difficulties with using Z production as a benchmark are: $m_Z \gg m_{\Upsilon_i}$ and the difference in the production mechanisms, $q\bar{q}$ and $qg + \bar{q}g$ for the Z and gg for $b\bar{b}$ production. The large m_Z reduces the value of Z production as a benchmark for two reasons. First, shadowing and related nuclear effects may be dependent upon Q^2, as in S_2 and S_3 [21, 18, 19]. Thus, it is possible that the shadowing at $Q^2 = m_{\Upsilon_i}^2$ will differ substantially from that at $Q^2 = m_Z^2$. Second, the x values probed ($x \sim m_Z/\sqrt{s} \sim 0.016$ at $y = 0$) are much larger than in Upsilon production at the same energy. In Fig. 9, one sees that $q\bar{q}$ collisions are dominant for $p_T \lesssim 15$ GeV while at higher p_T values $qg + \bar{q}g$ collisions dominate. Thus, to probe nuclear effects on the g distribution at $Q^2 = m_Z^2$, these effects on the q and $\bar{q}$ distributions at the same values of x and Q^2 must be understood. There is no direct measurement of q and $\bar{q}$ shadowing at small x with Q^2 values as high as m_Z^2. However, if nuclear beams become available at HERA, such measurements would be possible.

Given these issues, it would be advantageous if lepton pair production at $m_{\mu^+\mu^-} \approx m_{\Upsilon_i}$ could be to constrain shadowing and nuclear effects at parton x and Q^2 values closer to those of direct relevance. As already noted, a large background from $c\bar{c}$ and $b\bar{b}$ production processes is expected for $m_{\mu^+\mu^-} \leq m_{\Upsilon_i}$. At these low masses, this

---

[5] Thanks to U. Baur for providing a program against which to check these calculations.
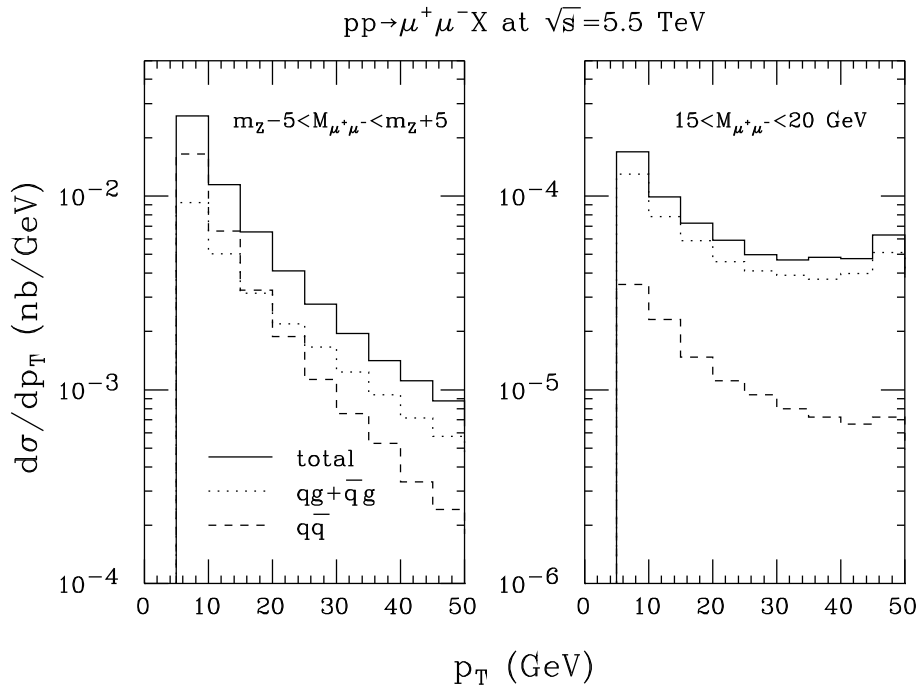
$$pp \to \mu^+\mu^- X \text{ at } \sqrt{s} = 5.5 \text{ TeV}$$

Figure 9: In (a), we plot $d\sigma/dp_T$ for $pp \to \mu^+\mu^- X$ at $\sqrt{s} = 5.5\,\text{TeV}$ as a function of p_T for Z production (defined by $m_Z - 5\,\text{GeV} \le M_{\mu^+\mu^-} \le m_Z + 5\,\text{GeV}$). In (b), the same cross section is plotted for $15\,\text{GeV} \le M_{\mu^+\mu^-} \le 20\,\text{GeV}$. The separate contributions from $q\bar{q}$ and $qg + \bar{q}g$ collisions are indicated by dashed and dotted histograms, respectively. From [34].

background will be very difficult to veto by requiring that the leptons be isolated because of the high density of soft tracks in the Pb+Pb collision environment. In the mass region above about $15\,\text{GeV}$ the dilepton rate from $c\bar{c}$ ($b\bar{b}$) pair production is predicted to be smaller than (comparable to) that from $\gamma^\star$, $Z^\star$-exchange [65]. Further, in this higher mass range, vetoing the $b\bar{b}$ component using isolation requirements on the leptons might prove feasible at a level adequate to extract the pure DY dilepton spectrum. In Fig. 9, $d\sigma/dp_T$ is given for production of muon pairs with $15\,\text{GeV} \le M_{\mu^+\mu^-} \le 20\,\text{GeV}$ coming from $\gamma^\star$, $Z^\star$-exchange. In this case the $qg + \bar{q}g$ collision component is always dominant, as would be desirable for learning as much about gluon shadowing as possible. However, the cross section is nearly a factor of 100 below that for production at the Z resonance, implying that statistics would be a factor of 10 worse. Even a year of running will not provide enough Pb+Pb luminosity to yield measurements that are sufficiently accurate to constrain the shadowing and nuclear effects at the needed level of $\lesssim 5 - 10\%$. Thus, the low rate and uncertainty regarding the ability to veto the $b\bar{b}$ background implies that it may not be possible to use lepton pairs below the Z mass to improve the understanding of nuclear effects on the gluon distribution. Nonetheless, the possibility of doing so should not be ignored and appropriate data, including event characteristics that might allow vetoing, should be collected.

5 Energy Loss

A dense parton system is expected to be formed in the early stage of relativistic heavy-ion collisions due to the onset of hard and semihard parton scatterings. Interactions among the produced partons in this dense medium will most likely lead to partial thermalization and formation of a quark-gluon plasma. It is thus important to study phenomenological signals of the early parton dynamics, a crucial step towards establishing the evidence of a strongly interacting initial system and its approach to thermal equilibrium. Therefore the energy loss of fast partons is a good probe of dense matter [66]. Three signals of this energy loss, dE/dx, are discussed: the effect on heavy quark decays and consequently, on the shape of the dilepton continuum, jet quenching and rapidity shifts in global event characteristics.

5.1 Heavy Quarks and the Dilepton Continuum

Since heavy-flavored mesons carry most of the heavy quark energy after hadronization, the energy lost by heavy quarks traveling through the quark-gluon plasma is directly reflected in the suppression of large p_T heavy-flavored

mesons. Previous work suggested that since the charm production cross section is large, charm decays would dominate the dilepton continuum for $2 < M < 10$ GeV [17] after random π and K decays had been subtracted. Therefore the dilepton yields could be used as an indirect measurement of the charm spectrum. However, this conclusion depends crucially on the hadronization mechanism, the acceptance of a real detector and the energy loss in the medium. Large invariant mass heavy quark pairs are suppressed by the energy loss. Thus dileptons from their decays are also suppressed [67, 68]. The treatment of the energy loss in the model is described [67, 68] followed by a discussion of how the $c\overline{c}$ and $b\overline{b}$ pairs are generated, hadronized and decayed. The effect observable by CMS is finally examined.

First, the phase space distribution of the heavy quarks and the space-time evolution of the dense matter must be specified. The matter has a longitudinal fluid velocity $v_z^F = z/t$ in the local frame [28], essentially the fluid velocity of free-streaming particles produced at $z = 0$ and $t = 0$. Transverse flow, which sets in later, is neglected and both the medium and the heavy quarks are assumed to be produced at $z = 0$, the same point at which expansion begins. Then, for any space-time point, (z, t), a heavy quark is in a fluid with the same longitudinal velocity. In the fluid rest frame, the heavy quark thus has momentum $(0, \vec{p}_T)$. Energy loss reduces the heavy quark momentum to $(0, \vec{p}_T{}')$ in the rest frame so that the momentum of the heavy quark changes from $(m_T \sinh y, \vec{p}_T)$ to $(m_T' \sinh y, \vec{p}_T{}')$ in the lab frame. Thus the heavy quark loses its transverse momentum but retains its rapidity because it follows the longitudinal flow.

To simplify the calculations, spherical nuclei of radius $R_A = 1.2 A^{1/3}$ are assumed so that in central collisions, the transverse area of the system is the area of the nucleus. For a heavy quark with a transverse path, l_T, and mean-free path, λ, in the medium, $\mu = l_T/\lambda$ gives the average number of scatterings. The actual number of scatterings, n, is generated from the Poisson distribution, $P(n, \mu) = e^{-\mu} \mu^n / n!$. This corona effect is particularly important for heavy quarks produced at the edge of the transverse plane of the collision. In the rest frame of the medium, the heavy quark then experiences momentum loss $\Delta p = n\lambda \, dE/dx$.

When a heavy quark loses most of its momentum in the fluid rest frame, it begins to thermalize with the dense medium. The heavy quark is considered to be thermalized if its final transverse momentum after energy loss, p_T', is smaller than the average transverse momentum of thermalized heavy quarks with a temperature T. These thermalized heavy quarks are then given a random thermal momentum in the rest frame of the fluid generated from the distribution $dN/d^3p \propto \exp(-E/T)$. The final momentum of the thermalized heavy quark is obtained by transforming back from the local fluid frame to the center-of-mass frame of the collision. The parameters used in the calculation are $dE/dx = -1$ GeV/fm, $\lambda = 1$ fm and $T = 150$ MeV. Note that larger values of dE/dx, both collisional and radiative have been recently suggested for heavy quarks in the high temperature environment of the LHC [69]. However, simulations at RHIC energies [67] suggest that once the heavy quarks are assumed to lose energy, the suppression of the heavy quark spectra appears as long as $|dE/dx| \geq \langle p_T \rangle / R_A$ where $\langle p_T \rangle$ is the average transverse momentum of the heavy quark which produces leptons inside the detector acceptance. At central rapidities with Pb beams and $\langle p_T \rangle = 3$ GeV, $\langle p_T \rangle / R_A \sim 0.4$ GeV/fm.

The momentum distribution of the $Q\overline{Q}$ pairs is generated with from PYTHIA 6.115 [70]. Initial and final state radiation effectively simulates higher-order contributions to heavy quark production so that the pair is no longer azimuthally back-to-back as at leading order[6]. The MRS D$-'$ [71] parton distribution functions are used to normalize the charm pair production cross section to 17.7 mb in pp collisions at $\sqrt{s} = 5.5$ GeV [17]. The number of $Q\overline{Q}$ pairs in a Pb+Pb collision at impact parameter $b = 0$ is obtained by multiplying the pp production cross section by the nuclear overlap,

$$N_{Q\overline{Q}} = \sigma_{Q\overline{Q}}^{pp} T_{\mathrm{PbPb}}(\mathbf{0}) \tag{27}$$

where $T_{\mathrm{PbPb}}(\mathbf{0}) = 30.4/\mathrm{mb}$. This scaling results in 540 charm pairs in a central Pb+Pb event. The $b\overline{b}$ production cross section is 224 μb in $\sqrt{s} = 5.5$ TeV pp collisions, extrapolating to 6.8 $b\overline{b}$ pairs in an average central Pb+Pb event. Although the energy loss experienced by bottom quarks may be different from that of charm quarks [69], the same parameters are used.

Only dileptons from correlated $Q\overline{Q}$ pair decays, $N_{ll}^{\mathrm{corr}} = N_{Q\overline{Q}} B^2(Q/\overline{Q} \to l^\pm X)$ are considered, *i.e.*, a single $Q\overline{Q}$ pair produces the dilepton. Dileptons from uncorrelated $Q\overline{Q}$ decays, which appear at higher invariant mass than the correlated decays due to their larger rapidity gap, will be particularly abundant for charm decays since $N_{ll}^{\mathrm{uncorr}} = N_{Q\overline{Q}} (N_{Q\overline{Q}} - 1) B^2(Q/\overline{Q} \to l^\pm X)$. In principle, the finite detector acceptance significantly reduces the uncorrelated rate and like-sign subtraction should remove most of the remainder. In practice however, full

---

[6] No shadowing has been included in these calculations.

subtraction will be difficult. Another problem arises from uncorrelated lepton pairs from a heavy quark and a background π or K decay. Treatment of this background could be a problem, especially since high p_T pions and kaons are also expected to experience energy loss.

In order to obtain the final meson distributions, the heavy quark distributions are convoluted with a fragmentation function. While a delta-function type of fragmentation is sufficient for low p_T hadroproduction [72, 73], high p_T heavy quarks should fragment according to the Peterson function [74], $D(z) \propto [z(1 - 1/z - \epsilon/(1-z))^2]^{-1}$ where $z = p_Q/p_H$ and $\epsilon_c = 0.06$ and $\epsilon_b = 0.006$ [75]. Note that the heavy quark quantities are denoted by Q while the heavy hadron formed from the fragmentation of the quark is denoted with H. A corresponding intrinsic k_T kick of 1 GeV for the partons in the proton is also included. In a high-energy collision, $\sqrt{s}/m \gg 1$, the heavy quark rapidity distribution is essentially flat. However, the hadronization of the heavy quark enhances the rapidity distribution at central rapidities. If the delta-function type of fragmentation is assumed, the momentum does not change but the rapidity shifts so that

$$dn \propto dy_Q = \frac{dp_{zQ}}{E_Q} = \frac{dp_{zH}}{E_Q} = \frac{\cosh y_H \, dy_H}{\sqrt{\cosh^2 y_H - \alpha^2}} \tag{28}$$

where

$$\alpha^2 = \frac{m_H^2 - m_Q^2}{m_{T,H}^2} \ . \tag{29}$$

For $m_c = 1.3$ GeV, $m_D = 1.87$ GeV and $m_{T,D} \approx \sqrt{2} m_D$, $\alpha^2 = 0.25$, enhancing the D distribution at $y = 0$ by $\approx 15\%$. When $m_b = 4.75$ GeV, $m_B = 5.27$ GeV and $m_{T,B} = \sqrt{2} m_B$, $\alpha^2 = 0.09$, enhancing the B distribution by $\approx 5\%$. The range of the enhancement is $|y_H| < 2.5$. If the Peterson function is used instead, α^2 increases,

$$\alpha^2 = \frac{m_H^2 - z^2 m_Q^2}{m_{T,H}^2} \ , \tag{30}$$

increasing the D enhancement at $y = 0$ to $\approx 30\%$ for $\langle z \rangle \approx 0.7$ and the B enhancement to $\approx 15\%$ for $\langle z \rangle \approx 0.85$. These $\langle z \rangle$ are typical for the Peterson function with the ϵ values given above. The fragmentation then tends to pile up heavy hadrons at central rapidities.

Since the CMS detector is sensitive to decays of charm quarks with $p_T > 20$ GeV, the charm spectrum was generated in two steps to obtain a sufficient number of high p_T charm quarks. First 10^5 normal $c\bar{c}$ pairs were generated followed by an equal number of $c\bar{c}$ pairs with a high p_T trigger such that the $c\bar{c}$ pair spectrum contains pairs with $p_{T,c} > 5$ GeV and $p_{T,\bar{c}} > 5$ GeV only. These high p_T $c\bar{c}$ pairs were then removed from the normal spectrum so that the resulting soft $c\bar{c}$ spectrum contains those pairs with $p_{T,c} < 5$ GeV or $p_{T,\bar{c}} < 5$ GeV. The relative weight of the high p_T spectrum is obtained from the ratio of the high p_T events to the total distribution. Because the b quarks have a harder p_T spectrum than charm quarks, such a proceedure is unnecessary for $b\bar{b}$ pairs.

The average branching ratios of $\overline{D} \to \mu X$ are $\approx 12\%$. The lepton energy spectrum from D meson semileptonic decays in PYTHIA 6.115 is consistent with the measurement of the MARK-III collaboration [76]. The b quarks are assumed to fragment into $B^-, \overline{B}^0, \overline{B}_s^0$ and Λ_b^0 with production percentages 38%, 38%, 11% and 13%, respectively. Single leptons from bottom decays can be categorized as primary and secondary leptons. Muons directly produced in the decay $B \to lX$ are primary while those indirectly produced, $B \to DX \to lY$, are secondary. Primary leptons have a harder energy spectrum than secondary leptons. A decaying b hadron mainly produces primary μ^- and secondary μ^+ although it can also produce a smaller number of primary μ^+ due to $B^0 - \overline{B}^0$ mixing. The branching ratios of the necessary B hadron decays are 9.30% to primary μ^-, 2.07% to secondary μ^-, 1.25% to primary μ^+, and 7.36% to secondary μ^+. The total number of dimuons from a $B\overline{B}$ decay can be readily estimated to be 0.020. Another important source of dimuons from bottom decays is the decay of a single bottom, $B \to Dl_1X \to l_1l_2Y$. The branching ratio for a single B meson to a dimuon is 0.906%, therefore this source gives 0.018 dimuons, comparable to the yield from a $b\bar{b}$ pair decay. These branching ratios [58] and energy spectra from PYTHIA 6.115 are consistent with measurements [77].

In Fig. 10 the single charm p_T distribution and the resulting dilepton invariant mass spectrum from correlated $D\overline{D}$ decays are shown without any phase space cuts. The spectra in Fig. 10 are normalized, as are all figures in this section, to a single central Pb+Pb event. The dashed curves are the generated spectra without energy loss while the solid curves are the distributions after energy loss. Thermalization of charm quarks that have lost most of their momentum causes the build-up at low p_T, as seen in Fig. 10(a). At higher values, a shift in p_T occurs but

these quarks are sufficiently energetic to escape the dense medium without being thermalized. A comparison of the dilepton spectra before and after energy loss, Fig. 10(b), would naively suggest that the overall effect is small. However, this impression is misleading because the spectrum is integrated over the entire phase space. Heavy quarks and antiquarks in a pair tend to be separated by a significant rapidity gap. This gap can cause the invariant mass of the subsequent lepton pair to also be large. However, once the finite detector geometries are included, the effect of energy loss becomes more dramatic.
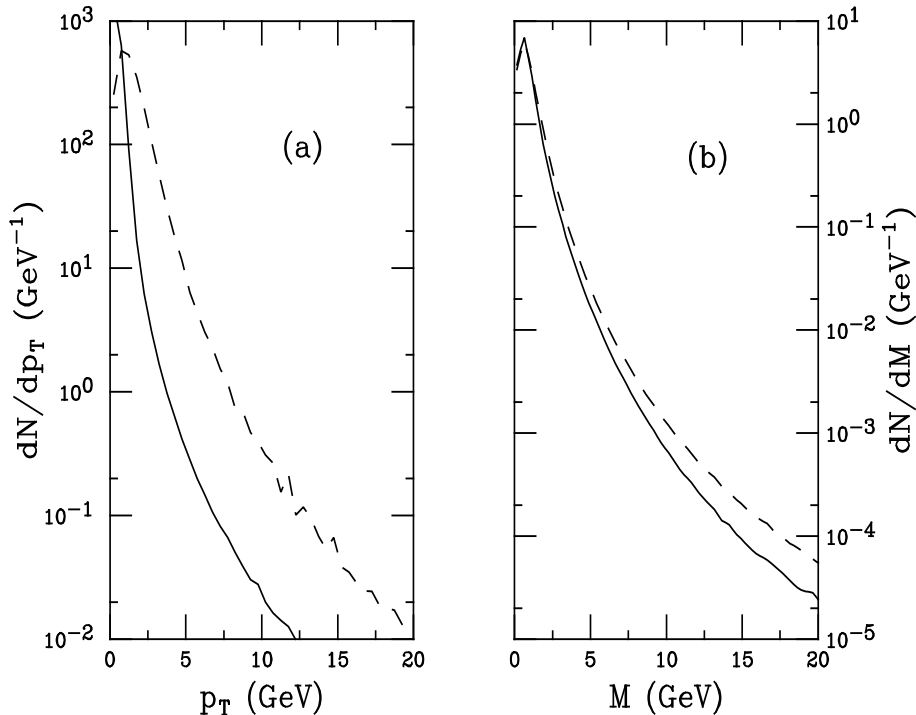

Figure 10: (a) The p_T distribution of single D mesons. (b) The invariant mass distribution of lepton pairs from correlated $D\overline{D}$ decays. Both distributions are integrated over all phase space. The dashed curves are results without energy loss, the solid curves include energy loss with $dE/dx = -1$ GeV/fm. From [68].

Figure 11 shows the corresponding single bottom p_T distribution and the integrated invariant mass spectra from correlated $B\overline{B}$ and single B decays. The dotted curve is the result of the decays of a single B to lepton pairs. When $M < 3$ GeV, this contribution is larger than the dilepton yield from $B\overline{B}$ decays, shown in the dot-dashed curve. Both include energy loss. The solid curve is the sum of the two contributions while the dashed curve is the sum of single and pair decays to dileptons without energy loss. The same trends are seen for bottom as well as charm except that the suppression of the spectrum due to energy loss begins at larger invariant mass. Note that the mass distribution in Fig. 11(b) is truncated to more clearly show the contribution from single B decay.

The CMS muon acceptance is in the range $|\eta| \leq 2.4$ with a lepton p_T cut of 3 GeV. After these simple cuts are applied, the results are shown in Fig. 12 for both $D\overline{D}$ and $B\overline{B}$ decays. Whereas for $M \leq 15$ GeV, the $D\overline{D}$ decays would dominate those of $B\overline{B}$ before the cuts, the measured $B\overline{B}$ decays are everywhere larger than those from charm mesons both before and after energy loss. The generally larger momentum of muons from B decays and the rather high momentum cut result in less acceptance loss for $B\overline{B}$ decays. No $D\overline{D}$ decay pairs with $M \leq 5$ GeV survive the momentum cut. A factor of 50 reduction in rate at $M \sim 10$ GeV is found before energy loss when comparing Figs. 12 and 10(b). A decrease in rate by a factor of 100 is obtained when energy loss is included. The corresponding loss of acceptance from $B\overline{B}$ decays is significantly less, a factor of ≈ 8 before energy loss and ≈ 15 when energy loss is included. Interestingly, the leptons in the decay chain of a single B meson are energetic enough for both to pass the momentum cut, causing the peak at $M \sim 2 - 3$ GeV. These results suggest that rather than providing an indirect measurement of the charm cross section, as postulated in [17], the dilepton continuum above the Υ family could instead measure the $b\overline{b}$ production cross section indirectly. A comparison with the spectrum from pp interactions at the same energy would then be sensitive to the amount of energy loss, dE/dx, of the medium.

A comparison of the p_T distributions of single muons in the CMS acceptance from the decays of D and B mesons can also provide a measure of the b cross section, shown in Fig. 13. When $p_T > 10 - 15$ GeV, the muon p_T
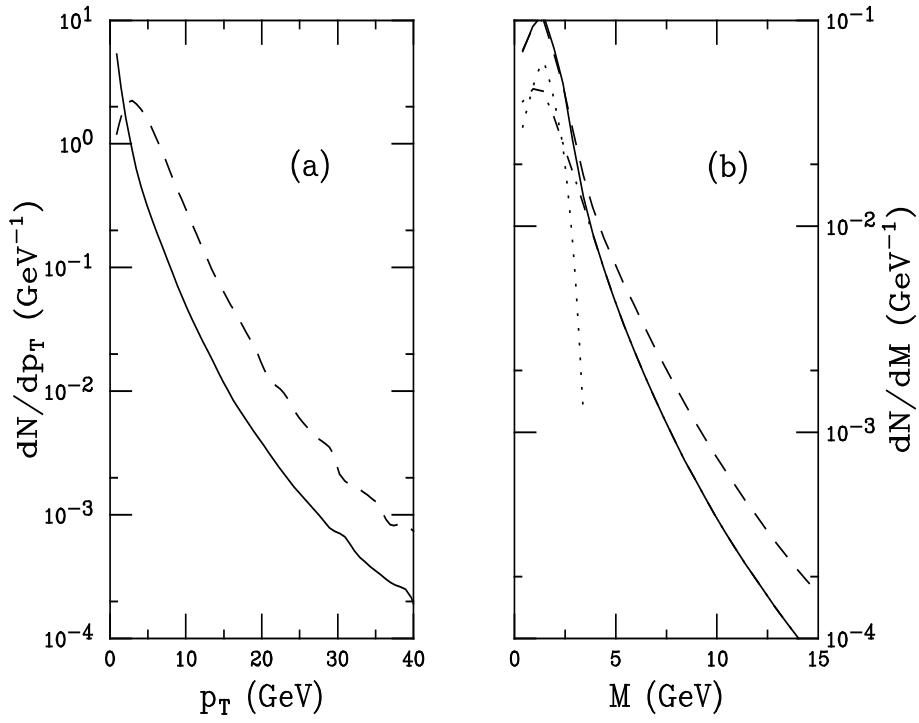
18

Figure 11: (a) The p_T distribution of single B mesons. (b) The invariant mass distribution of lepton pairs from correlated $B\overline{B}$ decays and single B decays. Both distributions are integrated over all phase space. The dotted curve is the contribution from semileptonic decay chains of single B mesons while the dot-dashed curve is from correlated $B\overline{B}$ decays. Both include energy loss. The dashed curves are results without energy loss, the solid curves include energy loss with $dE/dx = -1$ GeV/fm. Note that in (b), the dashed and solid curves include all single B and $B\overline{B}$ pair decays. From [68].
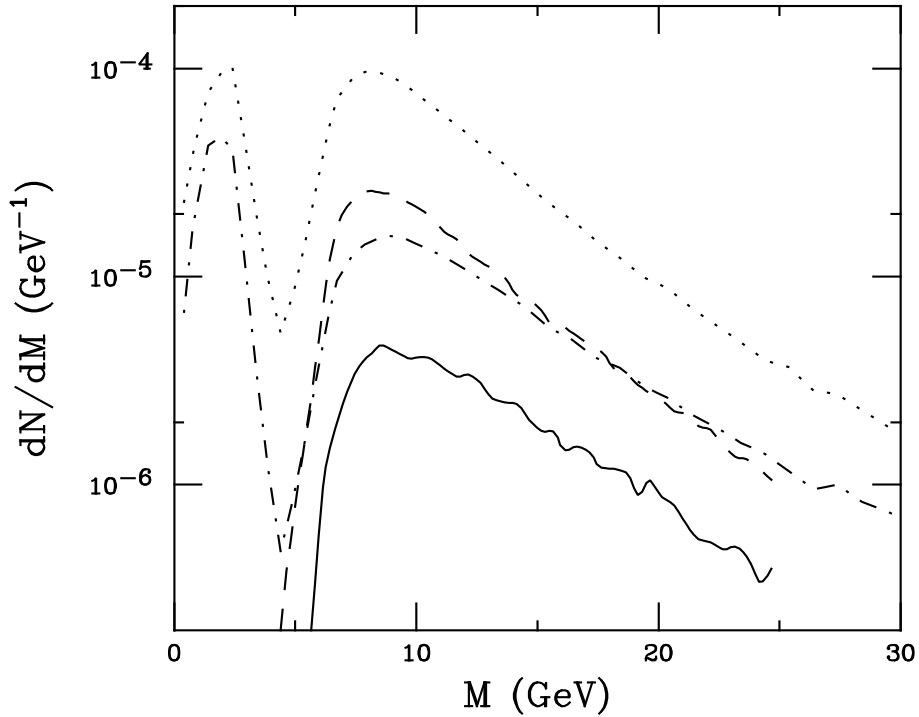

Figure 12: The dilepton invariant mass distribution in the CMS acceptance. The dashed and dotted curves are the $D\overline{D}$ and summed single B and $B\overline{B}$ decays respectively without energy loss. The solid and dot-dashed curves are the corresponding results with $dE/dx = -1$ GeV/fm. ¿From [68].

distribution is clearly dominated by B decays. This method of studying heavy quark production with single high p_T leptons was proposed as a measure of the charm rate at RHIC [78]. However, for this method to be viable, the background from random π and K decays must be well understood.
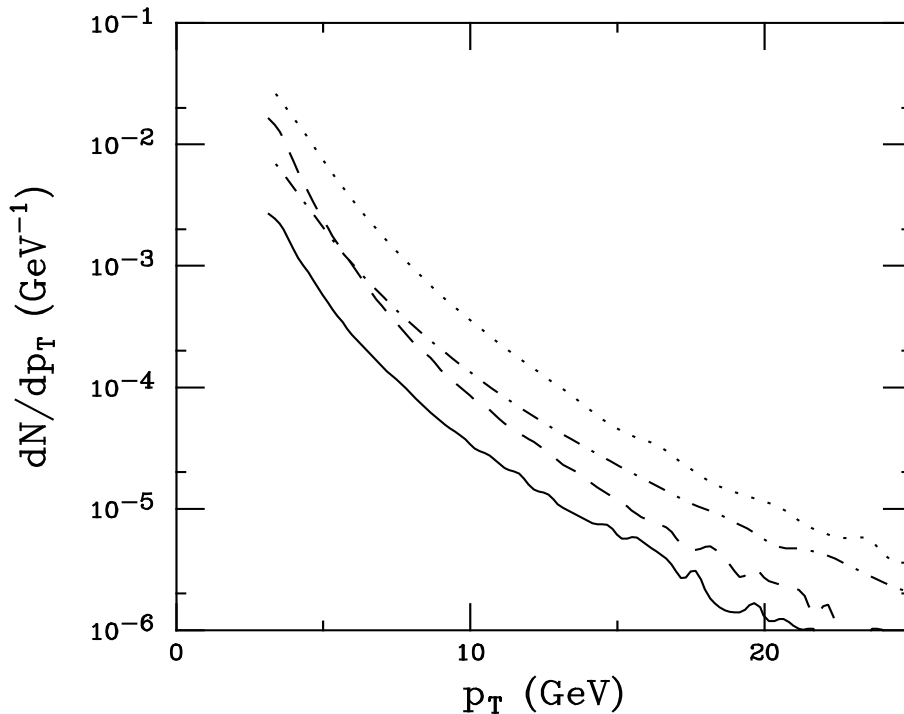

Figure 13: The single muon p_T distributions in the CMS acceptance. The dashed and dotted curves are the D and B meson decays respectively without energy loss. The solid and dot-dashed curves are the corresponding results with $dE/dx = -1$ GeV/fm. ¿From [68].

There are a number of uncertainties in the model. Although the relative formation times are neglected, the longitudinal velocity of heavy quarks and the fluid could be mismatched. The rapidity distribution of the heavy quarks is very sensitive to the flow pattern. The energy loss is assumed to be constant during the expansion of the system and the subsequent drop in the energy density. This need not necessarily be the case. Transverse flow, which could quantitatively change the low invariant mass dilepton yields, is also not included. However, the qualitative features of the results, such as the clear dominance of $b\bar{b}$ decays and the effect of energy loss when $|dE/dx| \geq \langle p_T \rangle / R_A$, are not likely to change.

5.2 Jet Quenching: The Monojet to Dijet Ratio

Jet quenching is a very good candidate for measuring energy loss since a fast parton traversing dense matter must experience multiple scatterings, or collisional energy loss, and also suffer radiative energy loss [79, 80, 81]. Two signatures of this energy loss in hard jet production addressed in this section are dijet quenching, a suppression of pairs of high p_T jets [82], and an enhancement of monojet production relative to the dijet rate [83]. The sensitivity of CMS to these signals for jets with transverse energy greater than 100 GeV was recently considered [84]. Other possible signatures that could directly measure the energy loss involve tagging the hard jet opposite a particle that does not interact strongly such as a Z boson [85] or a photon [86].

The total energy lost by a hard parton due to multiple scattering, ΔE_{tot}, is obtained by averaging over dijet production vertices (R, φ), the Q^2 of the rescattering, and the space-time evolution of the medium [87, 88]:

$$\Delta E_{\text{tot}} = \frac{1}{\sin\theta} \int\limits_0^{2\pi} \frac{d\varphi}{2\pi} \int\limits_0^{R_A} dR \, P_A(R) \int\limits_{\tau_0}^{\tau_L} d\tau \left(\frac{dE^{\text{rad}}}{dx}(\tau) + \frac{dE^{\text{coll}}}{dx}(\tau) \right) \tag{31}$$

where τ_0 and $\tau_L = \sqrt{R_A^2 - R^2 \sin^2\varphi} - R\cos\varphi$ are the QGP formation time and the time the jet escapes the plasma, respectively. Assuming a spherical nucleus, $P_A(R)$ is the distribution of distances R from the nuclear

collision axis to the dijet production vertex, $P_A(R) \approx 3(R_A^2 - R^2)/2R_A^3$ for $R \leq R_A$, and θ is the polar angle of the jet relative to the collision axis.

There are two contributions to the energy loss: dE^{rad}/dx is the radiative loss and dE^{coll}/dx is the collisional loss. The discussion here is restricted to the collisional loss, as in Refs. [87, 88]. Although the radiative energy loss is expected to dominate the collisional loss by up to an order of magnitude [79], there is no direct experimental verification of this loss. It was recently shown [80, 81] that the radiation of energetic gluons in a QCD medium is essentially different from the Bethe-Heitler independent radiation pattern since the formation time of such gluons exceeds their mean free path in the medium. Then coherent effects play a crucial role, leading to a strong suppression of medium-induced gluon radiation. This suppression is the QCD analogue of the Landau-Pomeranchuk-Migdal (LPM) effect in QED. The coherent LPM radiation induces a significant dependence of the jet energy on the jet cone size θ_0. Including radiative loss would increase ΔE_{tot} and thus enhance the proposed dijet quenching effect.

The collisional loss represents an incoherent sum over all rescatterings and is almost independent of the initial parton energy. Additionally, the angular distribution of the collisional energy loss is essentially different from that of the radiative loss. The majority of particles knocked out of the dense matter by elastic scatterings fly off transverse to the hard jet axis. As a result, the collisional energy loss is practically independent of θ_0. The contribution from the collisional loss could become significant for jets with finite cone size propagating through the plasma predicted in central heavy ion collisions.

The dijet production rate for jet pairs with individual jet transverse momenta p_{T_1} and p_{T_2} produced in the initial hard scatterings in central AA collisions is the result of averaging the total energy loss of each jet, eq.(31), over all dijet production vertices (R, φ),

$$
\frac{dN_{ij}^{\mathrm{dijet}}}{dy_1 dy_2 dp_{T_1} dp_{T_2}} = T_{AA}(\mathbf{0}) \int_0^{2\pi} \frac{d\varphi}{2\pi} \int_0^{R_A} dR P_A(R) \int dp_T^2 \frac{d\sigma_{ij}}{dp_T^2} \delta(p_{T_1} - p_T
$$
$$
+ \Delta E_{\mathrm{tot}}^i(\varphi, R)) \, \delta(p_{T_2} - p_T + \Delta E_{\mathrm{tot}}^j(\pi - \varphi, R)) \; . \tag{32}
$$

The jet cross section, $d\sigma_{ij}/dp_T^2$, is calculated in pp collisions using PYTHIA [70]

$$
\frac{d\sigma_{ij}}{dp_T^2} = K \int dx_1 \int dx_2 \int d\widehat{t} \, f_{i/p}(x_1, p_T^2) f_{j/p}(x_2, p_T^2) \frac{d\widehat{\sigma}_{ij}}{d\widehat{t}} \delta(p_T^2 - \frac{\widehat{t}\widehat{u}}{\widehat{s}}), \tag{33}
$$

where $d\widehat{\sigma}_{ij}/d\widehat{t}$ is parton-parton scattering cross section and $K \sim 2$ was used to account for higher order contributions. Shadowing is not included since it is not expected to be a strong effect in the x range of high E_T jets [84].

At leading order, hard jets are produced with $p_{T_1} = p_{T_2}$. A monojet is created from a dijet if one of the two hard jets loses so much energy that only a single jet is observable. This monojet rate is obtained by integrating the dijet rate over the transverse momentum p_{T_2} of the second (unobserved) jet for p_{T_2} smaller than the threshold value p_{cut}. Then the dijet rate, R^{dijet}, with p_{T_1}, $p_{T_2} > p_{\mathrm{cut}}$, and the corresponding monojet rate, R^{mono}, with $p_{T_1} > p_{\mathrm{cut}}$ and $p_{T_2} < p_{\mathrm{cut}}$, in central AA collisions at $y = 0$ is

$$
R_{AA}^{\mathrm{dijet}}(p_{T_1}, p_{T_2} > p_{\mathrm{cut}}) = \int_{p_{\mathrm{cut}}} dp_{T_1} \int_{p_{\mathrm{cut}}} dp_{T2} \int dy_1 dy_2 \sum_{i,j} \frac{dN_{ij}^{\mathrm{dijet}}}{dy_1 dy_2 dp_{T_1} dp_{T_2}} \; , \tag{34}
$$

$$
R_{AA}^{\mathrm{mono}}(p_{T_1} > p_{\mathrm{cut}}, p_{T_2} < p_{\mathrm{cut}}) = \int_{p_{\mathrm{cut}}} dp_{T_1} \int^{p_{\mathrm{cut}}} dp_{T2} \int dy_1 dy_2 \sum_{i,j} \frac{dN_{ij}^{\mathrm{dijet}}}{dy_1 dy_2 dp_{T_1} dp_{T_2}} \; . \tag{35}
$$

The dijet rate in AA relative to pp collisions can studied by introducing a reference process, unaffected by energy loss and with a rate proportional to the number of nucleon-nucleon collisions, such as Drell-Yan production,

$$
\frac{R_{AA}^{\mathrm{dijet}}}{R_{pp}^{\mathrm{dijet}}} = \frac{\sigma_{AA}^{\mathrm{dijet}}/\sigma_{pp}^{\mathrm{dijet}}}{\sigma_{AA}^{\mathrm{DY}}/\sigma_{pp}^{\mathrm{DY}}} \; , \tag{36}
$$

or Z production. This normalization is necessary to remove systematic errors in the luminosity. However, the ratio $R^{\mathrm{mono}}/R^{\mathrm{dijet}}$ does not need any external normalization since both rates can be measured simultaneously in AA

collisions, making such a study possible during a single run. A measurement relative to a reference process, as in eq. (36), requires pp and Pb+Pb runs at the same energy.

Three different assumptions of the collisional energy loss were studied in [88]: (i) no quenching; (ii) jet quenching in an ideal plasma where $\langle \Delta E_g \rangle \simeq 10$ GeV at $y = 0$ is obtained from eq. (31); (iii) jet quenching in a maximally viscous plasma with $C_\eta = 0.34$, resulting in $\langle \Delta E_g \rangle \simeq 20$ GeV at $y = 0$ [87]. The quark loss can be determined from the gluon loss by the ratio of color factors such that $\langle \Delta E_q \rangle = 4/9 \langle \Delta E_g \rangle$. A parton with energy E loses on average $\nu = \langle Q^2/2m_0 \rangle$ in a single elastic scattering with a parton of energy m_0 in the medium and also gets a transverse momentum kick $k_T = Q\sqrt{1 - \nu/E}$. The initial conditions for a gluon plasma in central Pb+Pb collisions were taken from Ref. [29], without shadowing.

The hard jet background is principally lower energy jets from secondary parton scatterings after the system has thermalized. This false jet background was simulated with a hydrodynamical model assuming $dN^\pm/dy|_{y=0} = 8000$ in the central unit of rapidity with $\langle p_T^\pi \rangle = 0.5$ GeV and $\langle p_T^K \rangle = 0.7$ GeV [88, 89]. Central Pb+Pb events are constructed from a superposition of the hydrodynamical model with the hard jet generated by PYTHIA in pp collisions [70].

To assess the CMS calorimeter response, some simplifying assumptions were made [88, 90]. Only the barrel calorimeter, $|\eta| < 1.5$, is included with a 4 T uniform magnetic field. The calorimeter cell size is 0.1×0.1 in $\eta - \phi$ with hadronic calorimeter resolution $\sigma/E = 70\%/\sqrt{E/\text{GeV}} + 1\%$ and electromagnetic calorimeter resolution $\sigma/E = 2\%/\sqrt{E/\text{GeV}} + 0.5\%$. The modified UA1 jet finding algorithm was used and only jets with $\langle R \rangle/R_{\text{jet}} < 0.5$ were accepted, where $R_{\text{jet}} = \sqrt{\Delta\eta^2 + \Delta\phi^2} = 0.5$ is the jet radius in $\eta - \phi$ space. The average jet radius is

$$\langle R \rangle = \sum_i R_{i_0}(E_i - \overline{E}_i)/E^{\text{jet}}, \quad E^{\text{jet}} = \sum_i (E_i - \overline{E}_i), \tag{37}$$

where R_{i_0} is the distance between cell i of the jet and the center of the jet, E_i and E^{jet} are the transverse energy in the cell and in the complete jet respectively, and $\overline{E}_i$ is the average cell transverse energy. A dijet is extracted from n-jet events by selecting the jet with the maximum transverse energy and because of the strong correlation, essentially back-to-back in azimuth, between the initial jet pair momenta, the jet opposite the first jet with the largest transverse energy was also selected:

$$\begin{aligned} E_{T,\text{jet}}^1 &= \max_{i=1,n} E_{T_i}, \\ E_{T,\text{jet}}^2 &= \max_{i=2,n} E_{T_i} \cos(\varphi_1 - \varphi_i - \pi). \end{aligned} \tag{38}$$

Figure 14 shows R^{dijet} as a function of the threshold jet energy E_T in central Pb+Pb collisions. An average jet radius $\langle R \rangle/R_{\text{jet}} < 1$ is assumed in (a) while $\langle R \rangle/R_{\text{jet}} < 0.5$ is used in (b). The probability of false dijet detection for $E_{\text{jet}}^{1,2} \geq E_T = 100$ GeV decreases by 2 orders of magnitude when the UA1 criteria is used. The contamination from false dijets, produced in secondary collisions, at threshold $E_T = 100$ GeV is about 25% in (a) and only $\sim 0.5\%$ in (b), decreasing rapidly with increasing threshold E_T. Thus the selection criterion on jet internal structure maximizes suppression of the false jet background. The hard dijet yield can be suppressed by up to a factor of ~ 7 due to collisional loss alone and could be even larger when radiative loss is included. The quenching is nearly independent of jet energy if the loss depends only weakly on the energy of the initial hard parton.

At luminosity $L_{\text{PbPb}} \simeq 1 \times 10^{27}$ cm^{-2}s^{-1} with $\sigma_{\text{PbPb}}^{\text{in}} \simeq 8$ b and a 3%-centrality trigger, there are $I_{\text{PbPb}}^{\text{central}} = 3\% L_{\text{PbPb}} \sigma_{\text{PbPb}}^{\text{in}} = 240$ events per second. Table 7 shows the hard dijet detection rates $H_{\text{PbPb}}^{\text{dijet}} = R_{\text{PbPb}}^{\text{dijet}} I_{\text{PbPb}}^{\text{central}}$, monojets $H_{\text{PbPb}}^{\text{mono}} = R_{\text{PbPb}}^{\text{mono}} I_{\text{PbPb}}^{\text{central}}$ and the monojet to dijet ratio $H^{\text{mono}}/H^{\text{dijet}}$ in the CMS barrel. The expected statistics should be sufficient to study high E_T jet production.

On the other hand, monojet detection and resolution are far from ideal. Initial state gluon radiation, finite calorimeter energy resolution, peculiarities of the jet finding algorithm, in addition to the background smears the observed hadronic jet characteristics relative to the initial partonic jet. In particular, there is a finite probability to register a jet with energy higher or lower than the initial jet, *i.e.* $p_{T_1} \neq p_{T_2}$, in contrast to the simple QCD picture of a single hard parton-parton scattering. As a consequence, $R^{\text{mono}}/R^{\text{dijet}} > 1$ even when no plasma is produced (see the lower solid line in Fig. 15) because of the smearing in $p_{T_1} - p_{T_2}$ at the parton level. Dijets with energy lower than the threshold energy E_T are partly transformed into monojets with energy higher than E_T while the reverse process is suppressed due to the sharp decrease of the initial dijet spectrum with energy, $\propto E_T^{-5}$. When energy loss in the plasma is included, $R^{\text{mono}}/R^{\text{dijet}}$ increases up to a factor of $1.5 - 2$ at $E_T \geq 100$ GeV over the rate in a

E_T (GeV)	100	150	200	250	300
no loss, $\langle \Delta E_g \rangle = 0$					
H^{dijet} (Hz)	1.0	1.5×10^{-1}	3.3×10^{-2}	1.0×10^{-2}	4.1×10^{-3}
H^{mono} (Hz)	6.3	8.0×10^{-1}	1.4×10^{-1}	3.6×10^{-2}	1.4×10^{-2}
$H^{\mathrm{mono}}/H^{\mathrm{dijet}}$	6.3	5.3	4.2	3.6	3.4
jet quenching in ideal QGP, $\langle \Delta E_g \rangle = 10$ GeV					
H^{dijet} (Hz)	3.1×10^{-1}	4.7×10^{-2}	1.2×10^{-2}	3.0×10^{-3}	1.0×10^{-3}
H^{mono} (Hz)	3.0	3.3×10^{-1}	6.9×10^{-2}	1.3×10^{-2}	5.2×10^{-3}
$H^{\mathrm{mono}}/H^{\mathrm{dijet}}$	9.7	7.0	5.7	4.2	5.2
jet quenching in viscous QGP, $\langle \Delta E_g \rangle = 20$ GeV					
H^{dijet} (Hz)	1.3×10^{-1}	2.1×10^{-2}	5.4×10^{-3}	1.8×10^{-3}	8.0×10^{-4}
H^{mono} (Hz)	1.7	2.1×10^{-1}	4.3×10^{-2}	1.1×10^{-2}	5.0×10^{-3}
$H^{\mathrm{mono}}/H^{\mathrm{dijet}}$	12.7	10.0	8.0	6.1	6.2

Table 7: The dijet ($E_T^{1,2} > E_T$) and monojet ($E_T^1 > E_T$) rates in central Pb+Pb collisions for $|\eta| < 1.5$.
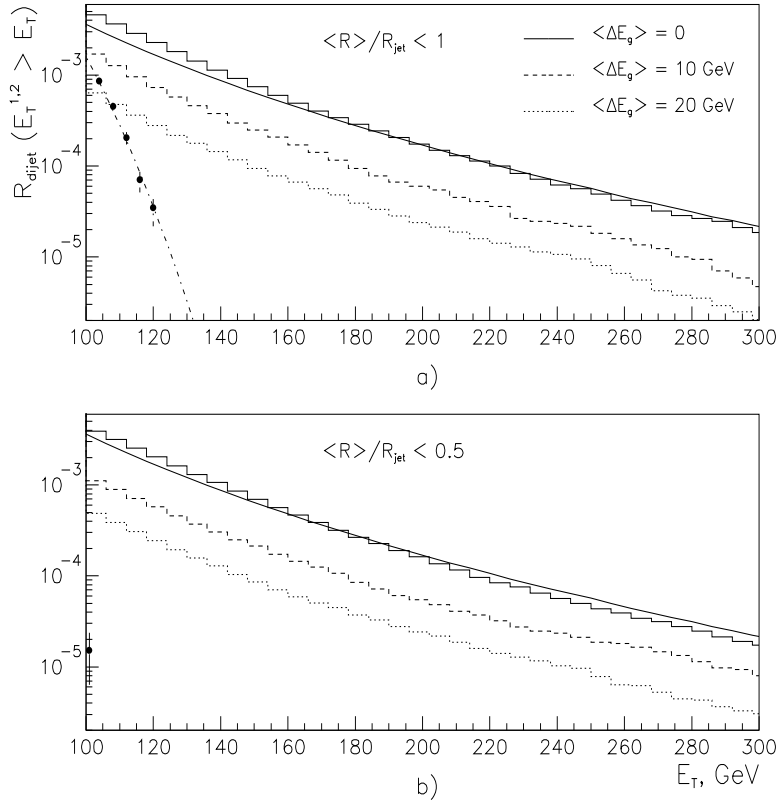

Figure 14: The dijet rate R_{dijet} with transverse energy $E_T^{1,2} > E_T$ in central Pb+Pb collisions for different quenching scenarios with true hard jets (histograms) compared to false jets (points with Gaussian fit, dot-dashed curve) from the hydrodynamic calculation with $dN^{\pm}/dy(y=0) = 8000$. The histograms represent $\langle \Delta E_g \rangle = 0$ (solid), 10 GeV (dashed), and 20 GeV (dotted). In (a) $\langle R \rangle / R_{jet} < 1$ is used while $\langle R \rangle / R_{jet} < 0.5$ is assumed in (b). The scaled PYTHIA result for the dijet spectrum is shown in the solid curve. From [84].

plasma without energy loss, a factor of $3 - 6$ above the baseline scaled PYTHIA result without plasma production, as also shown in Fig. 15.

Dijet production is more sensitive to the multiple scattering of jet partons in dense matter than the monojet yield which suffers from finite resolution and background effects. Studies of $R^{\mathrm{mono}}/R^{\mathrm{dijet}}$ can also provide additional information on the energy loss. Using the selection criteria $\langle R \rangle / R_{\mathrm{jet}} < 0.5$ maximizes the efficiency of true hard jet recognition while suppressing the false jet background.
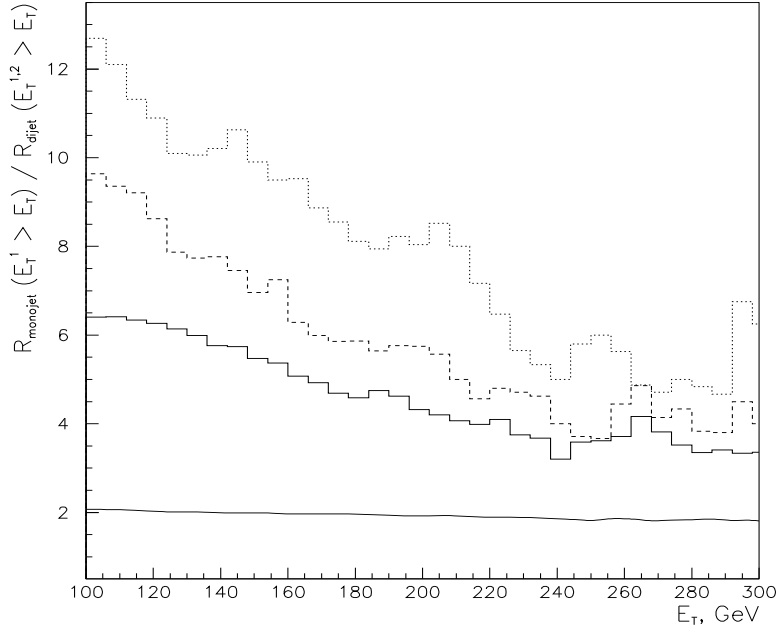
Figure 15: The monojet/dijet ratio as a function of the threshold jet energy E_T in central Pb+Pb collisions for different quenching scenarios and $\langle R \rangle / R_{jet} < 0.5$. The histograms represent $\langle \Delta E_g \rangle = 0$ (solid), 10 GeV (dashed), and 20 GeV (dotted). The scaled PYTHIA result for the dijet spectrum in shown in the solid curve. From [84].

5.3 Jet Quenching: Effects on Initial Conditions

CMS can also measure global event characteristics such as total transverse energy in the event, E_T, and the neutral and charged particle multiplicities, N_0 and $N_{\rm ch}$ [63]. These measurements would allow the correlation of plasma signals with event centrality in a meaningful way. The pseudorapidity coverage of the calorimeters, $-5 < \eta < 5$, will cover $\approx 80\%$ of $dE_T/d\eta$, providing a good measure of the global transverse energy. The energy loss by fast partons in matter, already discussed for heavy quarks [67, 68] and high transverse energy jets [84], would also modify global characteristics such as $dE_T/d\eta$. Studies [91] of radiative energy loss effects, proportional to the transverse distance traveled by a jet in the medium, using the HIJING event generator [92] indicate an enhancement in the range $|\eta| < 2$.

Fig. 16 shows $dE_T/d\eta$ for $\sim 1,000$ minimum bias Pb+Pb collisions at $\sqrt{s} = 5$ TeV/nucleon generated by HIJING in four different scenarios: no energy loss or nuclear shadowing; energy loss only; shadowing only; and the combined effect of shadowing and energy loss. A significant enhancement appears in the pseudorapidity range $|\eta| < 2$ when energy loss is included. Even peripheral Pb+Pb collisions show the effects of energy loss with the central enhancement still evident at impact parameters up to 12 fm [91]. Note that the shadowing parameterization used in HIJING reduces $dE_T/d\eta$ in the central region by a factor of ~ 2.6, larger than the decrease in $\overline{E}_T$ expected with more recent shadowing parameterizations and parton densities as shown in Table 1. This is perhaps because HIJING uses a simplified model of shadowing [92] along with the Duke-Owens parton densities [22]. Shadowing is included in all the HIJING simulations shown here.

The energy dependence of the enhancement in $dE_T/d\eta$ at central η is studied in Fig. 17. The results are given for Pb+Pb collisions at $\sqrt{s} = 5, 3, 1, 0.5, 0.2$, and 0.1 TeV/nucleon. The enhancement is observable above a central plateau when $\sqrt{s} > 0.5$ TeV/nucleon. At lower energies the effect is less pronounced because the rapidity gap between the projectile and target fragmentation regions is decreased. A study of the energy dependence thus requires a scan of $\sqrt{s}$ from a few hundred GeV/nucleon to several TeV/nucleon to survey the onset of the enhancement.

Since the LHC heavy ion injection system can provide sufficient luminosity for a variety of fully stripped nuclei with a short transition time between the injection of different ion types [93], it is possible to study the nuclear dependence of the energy loss. Because smaller nuclei require a shorter transverse distance for the partons to traverse before escaping the system, the effect must depend on system size. A scan of collisions of different nuclear systems provides an additional test of jet quenching. Thus HIJING was also used to simulate up to 10,000 minimum bias Nb+Nb, Ca+Ca, O+O, $\alpha + \alpha$, and pp interactions at $\sqrt{s} = 5$ TeV, compared to the Pb+Pb results in Fig. 18. The central enhancement due to energy loss decreases with system size as obvious from the comparisons

with and without energy loss.

The effect has only been shown for the global E_T distributions, $dE_T/d\eta$. However, qualitatively the same picture is seen when charged or neutral particle production is studied instead of E_T.
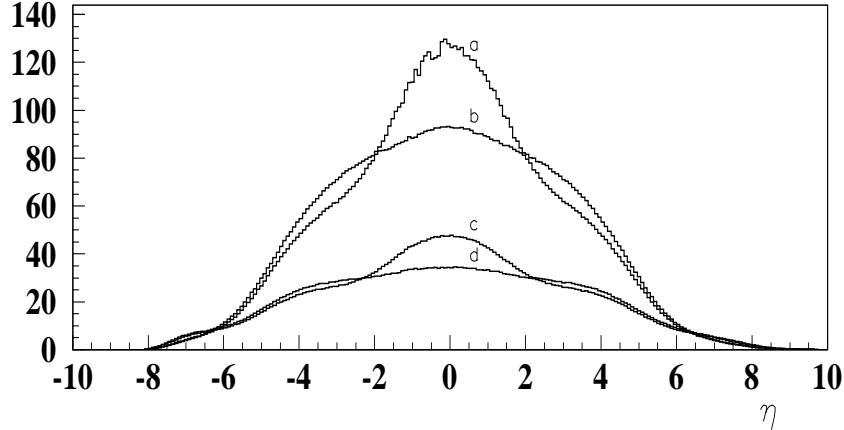

Figure 16: Modification of $dE_T/d\eta$ (GeV) as a function of η for 1,000 Pb+Pb collisions at $\sqrt{s} = 5$ TeV/nucleon normalized to the number of events with $d\eta = 0.087$ from the HIJING model. From top to bottom at $\eta = 0$ the curves are: (**a**) energy loss only, no shadowing; (**b**) no energy loss or shadowing; (**c**) energy loss and shadowing; (**d**) no energy loss, shadowing only. From [91].
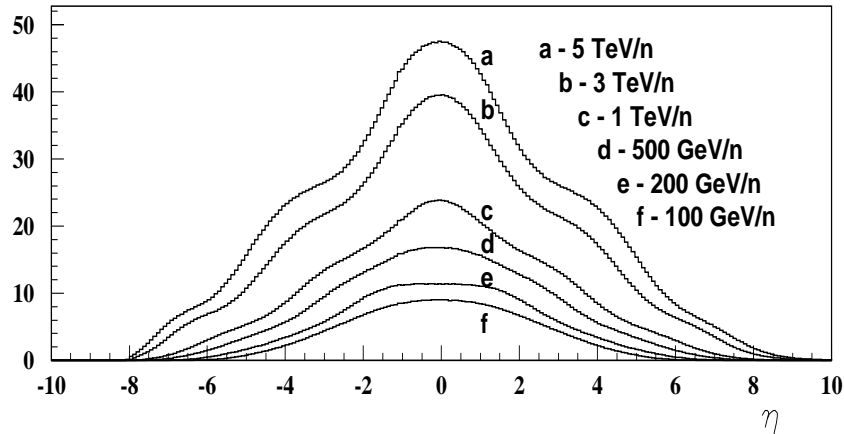

Figure 17: Total transverse energy as a function of η, $dE_T/d\eta$ (GeV), for Pb+Pb collisions at (from top to bottom) $\sqrt{s} = 5, 3, 1, 0.5, 0.2$, and 0.1 TeV/nucleon normalized to the number of events with $d\eta = 0.087$. The HIJING simulation includes both energy loss and shadowing. From [91].

The greater the energy loss, the more transverse energy is piled up at central η values, leading to an increase in energy density or 'stopping' in the central region, as has been seen at lower energies [95], in contradiction to the assumption of nuclear transparency [28]. Preliminary results indicate that the qualitively same results shown in Figs. 16-18 can be obtained using VENUS [94] with nucleon rescattering included. It is interesting to note that even though the physics of the VENUS rescattering mode is very different than that of the energy loss mechanism in HIJING, the end result is similar. This may be due to the fact that nucleon rescattering is also an effective form of nuclear 'stopping' [95]. The measurement of global characteristics can also provide an important correlation with collision centrality for signatures such as jet [84] and lepton pair production [34, 67, 68] as well as studies of the spatial dependence of the nuclear parton distributions [24].

This study demands a brief run with the solenoid switched off and variations in collision energy and system size. The availabilty of heavy ion beams when the CMS solenoid is not yet on is necessary to obtain undistorted distributions of total energy and charged multiplicity with η. Otherwise, distortions in the electromagnetic calorimeter due to charged hadron contamination must be shown to be small. In nucleus-nucleus collisions, normalization to pp collisions at the same energy would eliminate these systematic uncertainties. Only a relatively small sample of events is then needed to observe the enhancement, *e.g.* 100 Pb+Pb events was shown to be sufficient for observation of this central enhancement [96].
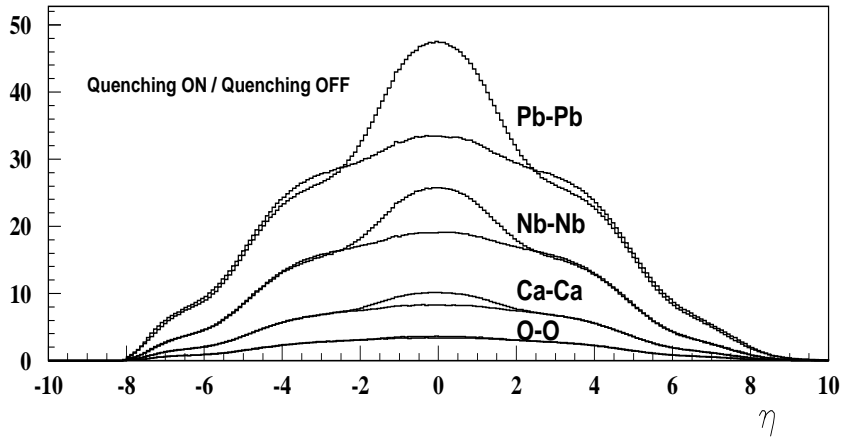
Figure 18: Total transverse energy as a function of η, $dE_T/d\eta$ (GeV) for (from top to bottom) Pb+Pb, Nb+Nb, Ca+Ca, and O+O collisions at $\sqrt{s} = 5$ TeV/nucleon with and without energy loss normalized to the number of events with $d\eta = 0.087$ from the HIJING model. All simulations include shadowing. From [91].

6 Summary

Some of the most prominent quark-gluon plasma signatures that could be studied with the CMS detector have been discussed here. Since the relative importance of these signatures depend on the initial conditions of the system, the role of minijet production in determining the initial conditions was described. Parton shadowing, which influences the initial temperature and the final multiplicity in an ideal quark-gluon plasma, was included. It was found that shadowing could reduce the initial temperature by decreasing the initial parton production. This reduction in the multiplicity would have the effect of making the environment easier to handle experimentally since the number of particles to be tracked would be reduced.

Quarkonium suppression through the Υ family is a promising signature, as already known from fixed-target experiments at the CERN SPS [5]. The p_T dependence of the Υ'/Υ ratio, as measured by CMS, could provide valuable information on the initial conditions of the plasma. As was shown, the initial conditions and the subsequent expansion of the system strongly influence the Υ'/Υ ratio. The Υ production rate is large enough for such measurements to be feasible. The ψ'/ψ ratio as a function of p_T can provide additional important information on the plasma even at high p_T.

Energy loss effects such as the modification of the dilepton continuum through heavy quark decays and jet quenching will provide complementary information on the density of the medium traversed by the hard partons as well as the influence of energy loss on global variables. The size of the energy loss influences the relative charm and bottom contribution to the dilepton continuum and the monojet to dijet ratio at high E_T. Both effects are observable by CMS. The CMS detector is particularly well suited for measuring high E_T jets.

Finally, it is important to note that any conclusions regarding quark-gluon plasma production depend on correlating as many signatures as possible. To understand the systematics of plasma production, studies of other systems at more than one energy will be crucial. To establish a baseline, pp and pPb collisions at the same energy as the Pb+Pb collisions are strongly advised. Going down in energy to *e.g.* the Tevatron energy of 1.8 TeV could provide an important cross check. Comparison of the Pb+Pb results with other nuclear systems such as Ca+Ca will also be important for a study of finite volume effects. Another necessary cross check for CMS will be comparison with results from the dedicated heavy-ion detector ALICE whenever possible since controversial results require confirmation, as already evident from the fixed-target heavy-ion program. Lessons learned from the CERN SPS heavy-ion program and the lower energy collider studies at RHIC should be put to good use as well.

References

[1] F. Karsch, Nucl. Phys. **A590** (1995) 367c.

[2] For the latest data on heavy ion collisions at the AGS and the SPS, see the Proceedings of the 13$^{\rm th}$ International Conference on Ultra-Relativistic Nucleus-Nucleus Collisions, Tsukuba, Japan, 1997.

[3] *Conceptual Design for the Relativistic Heavy Ion Collider*, BNL-52195, May, 1989, Brookhaven National Laboratory.

[4] ALICE Technical Proposal, CERN/LHCC/95-71 (1995); ALICE Addendum to the Technical Proposal, CERN/LHCC/96-32 (1996); A. Morsch *et al.* (ALICE Collab.), in Proceedings of the 13th International Conference on Ultra-Relativisitic Nucleus-Nucleus Collisions, Tsukuba, Japan, 1997.

[5] M.C. Abreu *et al.* (NA50 Collab.), Phys. Lett. **B410** (1997) 327, 337.

[6] R. Vogt, LBNL-41758, Physics Reports in press.

[7] D.M. Alde *et al.*, Phys. Rev. Lett. **66** (1991) 2285.

[8] T.K. Gaisser and F. Halzen, Phys. Rev. Lett. **54** (1985) 1754; L. Durand and H. Pi, Phys. Rev. Lett. **58** (1987) 303; G. Pancheri and Y.N. Srivastava, Phys. Lett. **B182** (1986) 199.

[9] C. Albajar *et al.* (UA1 Collab.), Nucl. Phys. **B309** (1988) 405.

[10] K.J. Eskola and M. Gyulassy, Phys. Rev. **C47** (1993) 2329.

[11] K.J. Eskola and K. Kajantie, Z. Phys. **C75** (1997) 515; K.J. Eskola, K. Kajantie and J. Lindfors, Nucl. Phys. **B323** 37 (1989).

[12] I. Abt *et al.* (H1 Collab.), Nucl. Phys. **B407** (1993) 515; M. Derrick *et al.* (ZEUS Collab.), Phys. Lett. **B316** (1993) 412.

[13] M. Glück, E. Reya, and A. Vogt, Z. Phys. **C67** 433, (1995).

[14] A.D. Martin, R.G. Roberts and W.J. Stirling, Phys. Lett. **B354** 155, (1995).

[15] K.J. Eskola and X.-N. Wang, Int. J. Mod. Phys. **A10** (1995) 2881.

[16] J.J. Aubert *et al.*, Nucl. Phys. **B293** 740, (1987); M. Arneodo, Phys. Rep. **240** 301, (1994).

[17] S. Gavin, P.L. McGaughey, P.V. Ruuskanen and R. Vogt, Phys. Rev. **C54** 2606, (1996).

[18] K.J. Eskola, V.J. Kolhinen and P.V. Ruuskanen, CERN-TH/97-345, JYFL-2/98 and hep-ph/9802350, Nucl. Phys. **B** in press.

[19] K.J. Eskola, V.J. Kolhinen and C.A. Salgado, JYFL-8/98, US-FT/14-98, hep-ph/9807297.

[20] K.J. Eskola, J. Qiu, and J. Czyzewski, private communication.

[21] K.J. Eskola, Nucl. Phys. **B400** 240, (1993).

[22] D.W. Duke and J.F. Owens, Phys. Rev. **D30** (1984) 49.

[23] M. Glück, E. Reya, and A. Vogt, Z. Phys. **C53** (1992) 127.

[24] V. Emel'yanov, A. Khodinov, S.R. Klein and R. Vogt, Phys. Rev. **C56**, 2726 (1997); Phys. Rev. Lett. **81** (1998) 1801.

[25] V. Emel'yanov, A. Khodinov, S.R. Klein and R. Vogt, in progress.

[26] K.J. Eskola, R. Vogt, and X.-N. Wang, Int. J. Mod. Phys. **A10** (1995) 3087.

[27] C.W. deJager, H. deVries, and C. deVries, Atomic Data and Nuclear Data Tables **14** 485, (1974).

[28] J.D. Bjorken, Phys. Rev. **D27** (1983) 140.

[29] K.J. Eskola, K. Kajantie and P.V. Ruuskanen, Phys. Lett. **B332** (1994) 191.

[30] H. Satz, Nucl. Phys. **A544** (1992) 371c.

[31] T. Matsui and H. Satz, Phys. Lett. **B178** (1986) 416.

[32] F. Karsch, M.T. Mehr, and H. Satz, Z. Phys. **C37** (1988) 617.

[33] F. Karsch and H. Satz, Z. Phys. **C51** (1991) 209.

[34] J.F. Gunion and R. Vogt, Nucl. Phys. **B492** (1997) 301.

[35] D.J. Gross, R.D. Pisarski, and L.G. Yaffe, Rev. Mod. Phys. **53** (1981) 43.

[36] P. Levai and U. Heinz, Phys. Rev. **C57** (1998) 1879.

[37] G. Boyd *et al.*, Nucl. Phys. **B469** (1996) 419.

[38] J. Fingberg, U.M. Heller and F. Karsch, Nucl. Phys. **B392** (1993) 493.

[39] U.M. Heller, F. Karsch and J. Rank, Phys. Lett. **B355** (1995) 511.

[40] B. Petersson, Nucl. Phys. **A525** (1991) 237c.

[41] For a review, see G. Schuler, CERN Preprint CERN-TH.7170/94, February 1994 and references therein.

[42] M.L. Mangano, P. Nason and G. Ridolfi, Nucl. Phys. **B405** (1993) 507.

[43] R.V. Gavai *et al.*, Int. J. Mod. Phys. **A10** (1995) 3043.

[44] G.A. Schuler and R. Vogt, Phys. Lett. **B387** (1996) 181.

[45] A. Sansoni (CDF Collab.), Nucl. Phys. **A610** (1996) 373c.

[46] L. Antoniazzi *et al.*, Phys. Rev. Lett. **70** (1993) 383.

[47] L. Antoniazzi *et al.*, Phys. Rev. **D46** (1992) 4828.

[48] B. Ronceux, NA38 Collab., Nucl. Phys. **A566** (1994) 371c.

[49] J.K. Yoh *et al.*, Phys. Rev. Lett. **41** (1978) 684; K. Ueno *et al.*, Phys. Rev. Lett. **42** (1979) 486.

[50] T. Yoshida *et al.*, Phys. Rev. **D39** (1989) 3516.

[51] G. Moreno *et al.*, Phys. Rev. **D43** (1991) 2815.

[52] F. Abe *et al.* (CDF Collab.), Phys. Rev. Lett. **75** (1995) 4358.

[53] S.J. Brodsky, C. Peterson and N. Sakai, Phys. Rev. **D23** (1981) 2745; S.J. Brodsky, P. Hoyer, C. Peterson and N. Sakai, Phys. Lett. **93B** (1980) 451.

[54] E. Braaten, M.A. Doncheski, S. Fleming and M.L. Mangano, Phys. Lett. **B333** (1994) 548.

[55] J. Badier *et al.*, Phys. Lett. **86B** (1979) 98; S. Childress *et al.*, Phys. Rev. Lett. **55** (1985) 1962.

[56] D. Antreasyan *et al.*, Phys. Rev. Lett. **45** (1980) 863; C. Kourkoumelis *et al.*, Phys. Lett. **91B** (1980) 481; A.L.S. Angelis *et al.*, Phys. Lett. **87B** (1979) 398.

[57] C. Albajar *et al.*, Phys. Lett. **B186** (1987) 237.

[58] Particle Data Group, R.M. Barnett *et al.*, Phys. Rev. **D54** (1996) 1.

[59] D.M. Alde *et al.* (E772 Collab.), Phys. Rev. Lett. **66** (1991) 2285.

[60] X.-M. Xu, D. Kharzeev, H. Satz and X.-N. Wang, Phys. Rev. **C53** (1996) 3051.

[61] D. Kharzeev and H. Satz, Phys. Lett. **B366** (1996) 316.

[62] J. Ftaćnik, P. Lichard, J. Pišút, Phys. Lett. **B207** (1988) 194; S. Gavin, M. Gyulassy and A. Jackson, Phys. Lett. **B207** (1988) 257; R. Vogt, M. Prakash, P. Koch and T.H. Hansson, Phys. Lett. **B207** (1988) 263; J. Ftaćnik, P. Lichard, N. Pišútova and J. Pišút, Z. Phys. **C42** (1989) 132.

[63] CMS Technical Proposal, CERN/LHCC 94-38 (1994).

[64] S. Ramos *et al.*, NA38 Collab., Nucl. Phys. **A590** (1995) 117c and references therein.

[65] These statements are based on the calculations of Ref. [17] for the LHC (using the acceptances of the ALICE experiment).

[66] X.-N. Wang and M. Gyulassy, Phys. Rev. Lett. **68** (1992) 1480.

[67] Z. Lin, R. Vogt and X.-N. Wang, Phys. Rev. **C57** (1998) 899.

[68] Z. Lin and R. Vogt, LBNL-42096, hep-ph/9808214.

[69] M.G. Mustafa, D. Pal, D.K. Srivastava and M.H. Thoma, nucl-th/9711059.

[70] T. Sjöstrand, Comput. Phys. Commun. **82** (1994) 74. Further program updates and documentation can be found at *http://www.thep.lu.se/tf2/staff/torbjorn/Pythia.html*.

[71] A.D. Martin, W.J. Stirling and R.G. Roberts, Phys. Lett. **B306** (1993) 145; erratum-ibid. **B309** (1993) 492.

[72] R. Vogt, S.J. Brodsky and P. Hoyer, Nucl. Phys. **B383** (1992) 643.

[73] E769 Collaboration, Phys. Rev. Lett. **77** (1996) 2392.

[74] C. Peterson, D. Schlatter, I. Schmitt, and P. Zerwas, Phys. Rev. **D27** (1983) 105.

[75] J. Chirn, in *Proc. Int. Symp. on Production and Decay of Heavy Flavors*, Stanford, California, 1987, edited by E. Bloom and A. Fridman, p. 131.

[76] R.M. Baltrusaitis *et al* (MARK-III Collab.), Phys. Rev. Lett. **54** (1985) 1976; erratum-ibid. **55** (1985) 638.

[77] S. Behrends *et al* (CLEO Collab.), Phys. Rev. Lett. **59** (1987) 407; **76** (1996) 1570.

[78] M. Tannenbaum, Heavy Ion Phys. **4** (1996) 139.

[79] M. Gyulassy and X.-N. Wang, Nucl. Phys. **B420** (1994) 583; X.-N. Wang, M. Gyulassy and M. Plumer, Phys. Rev. **D51** (1995) 3436.

[80] R. Baier, Yu.L. Dokshitser, S. Peigne and D. Schiff, Phys. Lett. **B345** (1995) 277.

[81] R. Baier, Yu.L. Dokshitser, A.H. Mueller, S. Peigne and D. Schiff, Nucl. Phys. **B478** (1996) 577; **B483** (1997) 291; **B484** (1997) 265.

[82] M. Gyulassy and M. Plumer, Phys. Lett. **B234** (1990) 432.

[83] M. Plumer, M. Gyulassy and X.-N. Wang, Nucl. Phys. **A590** (1995) 511.

[84] I.P. Lokhtin, L.I. Sarycheva, A.M. Snigirev and I.N. Vardanyan, CERN CMS TN 1998/025.

[85] V. Kartvelishvili, R. Kvatadze and R. Shanidze, Phys. Lett. **B356** (1995) 589.

[86] X.-N. Wang, Z. Huang, and I. Sarcevic, Phys. Rev. Lett. **77** (1996) 231.

[87] I.P. Lokhtin and A.M. Snigirev, Phys. At. Nucl. **60** (1997) 360; Z. Phys **C73** (1997) 315.

[88] N.A. Kruglov *et al.*, CERN CMS TN 1996/083; CERN CMS TN 1996/084.

[89] N.A. Kruglov, I.P. Lokhtin, L.I. Sarycheva, A.M. Snigirev, Z. Phys. **C76** (1997) 99.

[90] V.L. Korotkikh *et al.*, CERN CMS TN 1994/244.

[91] M.V. Savina, S.V. Shmatov, N.V. Slavin, and P.I. Zarubin, private communication.

[92] X.-N. Wang and M. Gyulassy, Phys. Rev. **D44** (1991) 3501; **D45** (1992) 844.

[93] D. Brandt, K. Eggert, and A. Morsch, CERN AT/94-05(DI), SL/94-04(AP), LHC Note 264.

[94] K. Werner, Phys. Reports **232** (1993) 87.

[95] J. Baechler *et al.* (NA49 Collab.), Phys. Rev. Lett. **72** (1994) 1419; T. Wienold *et al.* (NA49 Collab.), Nucl. Phys. **A610** (1996) 76c.

[96] V. Genchev, N.V. Slavin, V.V. Uzhinskii, and P.I. Zarubin, CMS Internal Note 97-10.